Structural and magnetic properties of ultrathin Ni/Fe bilayers grown epitaxially on Ag(001)

B. Heinrich, S. T. Purcell, J. R. Dutcher, K. B. Urquhart,
J. F. Cochran, and A. S. Arrott
Department of Physics, Simon Fraser University, Burnaby, British Columbia, Canada V5A 1S6
(Received 12 July 1988)

Ultrathin epitaxial single bilayers of Ni/Fe were grown on Ag(001) substrates by means of molecular-beam epitaxy. The growths were monitored by reflection high-energy electron diffraction, x-ray photoemission, and Auger-electron spectroscopies. The Ni grows in the pure bcc structure for the first 3–6 monolayers and then reconstructs into a modified bcc phase for larger Ni thicknesses. The magnetic properties of the bilayers were studied using ferromagnetic resonance and Brillouin light scattering. The pure bcc Ni overlayers have no effect on the magnetic properties of the ultrathin Fe layers. Reconstructed Ni overlayers create a large in-plane anisotropy with fourfold symmetry in the bilayers with the easy axis along the Fe[100] crystallographic direction. A theory of exchange-coupled layers is presented. It is shown that for strongly exchange-coupled layers the bilayer magnetic properties are given by a linear combination of the magnetic properties of the individual layers, with coefficients for each layer given by the product of the magnetic moment per atom and the number of monolayers. The fourfold anisotropy agrees well with the bilayer theory and its value can be controlled by the appropriate choice of the individual layer thicknesses. These large in-plane anisotropies with fourfold symmetry are not common in 3*d* transition metals and it is unique that they are a result of misfit dislocations created during the Ni lattice reconstruction.

I. INTRODUCTION

An exciting aspect of molecular-beam epitaxy (MBE) is the ability to grow new magnetic materials. In this paper we present our recent results on the growth by MBE of ultrathin bilayers consisting of "bcc Ni" on bcc Fe.[1] They are grown on Ag(001) substrates and their magnetic properties were studied using ferromagnetic resonance (FMR) and Brillouin light scattering (BLS). The ultrathin Ni/Fe bilayers form new materials with unique magnetic properties of their own.

The interpretation of our results relies on previous work carried out on ultrathin[2] layers of bcc Fe epitaxially grown on fcc Ag(001) substrates[3,4] and ultrathin "bcc Ni" epitaxially grown on bulk bcc Fe(001).[5,6] We begin with a brief review of these previous studies.

bcc Fe films epitaxially grown on Ag(001) substrates have attracted considerable interest[3–4,7–12] due to their strong perpendicular anisotropy which, in some instances, results in the saturation magnetization M_s pointing perpendicular to the specimen surface in zero applied field.

FMR experiments carried out on ultrathin Ni(001) layers epitaxially deposited on bulk Fe(001) substrates revealed that Ni overlayers exhibit a large in-plane cubic magnetic anisotropy ($2K_1/M_S \approx 3$ kOe).[5,6] The magnetic response of these samples was dominated by the Fe substrates and weakly modified by the Ni overlayers. In the first approximation the magnetization of the Ni overlayer is constant across the layer and follows the magnetization of the Fe at the interface due to strong exchange coupling. This results in dynamic surface pinning of the Fe. Detailed theoretical[13] and computer calculations[6] were carried out and compared with FMR results. A unique interpretation of the FMR results was hard to achieve due to complexities arising from a strong dependence of the dynamic surface pinning on all Ni-overlayer magnetic parameters. Fortunately, a noticeably large inplane angular dependence of the dynamic surface pinning allowed us to identify and estimate fairly well the value of the cubic magnetic anisotropy of "bcc Ni" ($2K_1/M_s \approx 3$ kOe).

Most of these complexities can be avoided by replacing the bulk Fe substrate with ultrathin Fe films epitaxially grown on bulk Ag(001) substrates. Such Fe films have suitable surfaces for epitaxial growth, as determined by reflection high-energy electron diffraction (RHEED) (see Fig. 1). Our initial goal was to learn more about the magnetic properties of the "bcc Ni." To extract the magnetic parameters of the "bcc Ni" from the bilayer data the theory of bilayer magnetic properties was formulated in terms of the magnetic properties of the individual layers. A simple theory was developed which assumed two layers with uniform magnetization within a layer and interacting at their interface. We expanded our calculations to include the description of optical modes in which exchange interactions between atomic planes play a dominant role. We have found some of these results stimulating and worth reporting in themselves.

This paper is organized as follows. In Sec. II the growth studies and structural properties of "bcc Ni" overlayers grown on bulk Fe and ultrathin bcc Fe film substrates are discussed. Section III describes the scaling laws valid for the homogeneous precession mode and discusses optical modes. Experimental results are presented in Sec. IV, followed by their interpretation in Sec. V. The main theoretical and experimental results are summarized in Sec. VI.

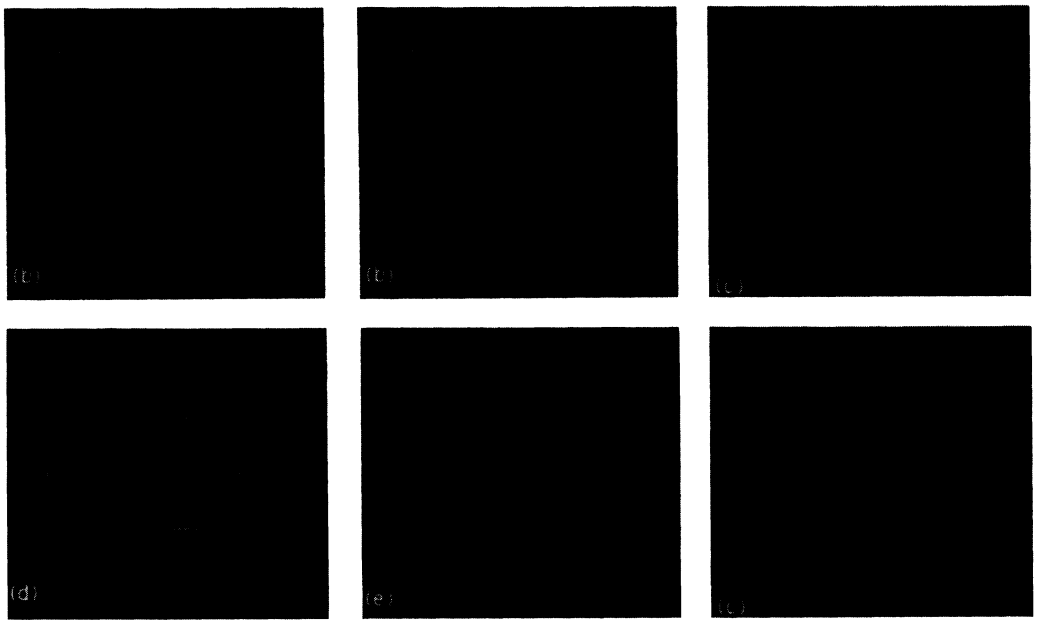

FIG. 1. RHEED patterns from 5.6 ML of Fe on Ag(001) [(a)–(c)] and 3.5 ML of Ni on the 5.6 ML Fe on Ag(001) [(d)–(f)]. The incident electron beam (10 kV) is along the Fe[100] azimuth in photos (a) and (d), the Fe[110] azimuth in (b) and (e), and the Fe [120] in (c) and (f). The RHEED photos show the surface to be a square array having the bulk Fe lattice spacing. The Ni on Fe on Ag patterns are almost identical to the Fe on Ag patterns with no extra diffraction streaks.

II. PREPARATION AND GROWTH STUDIES OF ULTRATHIN FILMS

The epitaxial growth of ultrathin films was carried out in a Physical Electronics molecular-beam epitaxy (Φ MBE-400) system. This MBE system is equipped with (RHEED) and an angularly resolved double-pass cylindrical mirror analyzer (CMA) for Auger-electron (AES) and x-ray photoelectron (XPS) spectroscopies. The film growth is monitored *in situ* by RHEED. The sample surface can be rotated 360° with respect to the RHEED electron beam allowing one to study the full azimuthal dependence of the RHEED patterns. The RHEED screen is equipped with a magnifying lens to focus a small section of the screen onto a photomultiplier tube permitting us to measure the intensity of the RHEED specular spot as a function of film thickness.

The Ag(001) substrates were 15 mm in diameter and 3.5 mm thick. They were spark cut from a single crystal boule with a mosaic spread of ≈ 20 mrad. The substrates were ground and polished mechanically before a final electropolish with a cyanide-free solution[14] which produced a strain-free, smooth, mirrorlike surface. The Ag substrates were sputter etched with an Ar^+-ion beam at 2 keV and 8 $\mu A/cm^2$ for 30 min. The surface damage induced by ion milling was removed by annealing at 450 °C in ultrahigh vacuum (low 10^{-10} Torr range) for 20 min. The preparation of bulk Fe substrates used in our growth studies has been described in detail elsewhere.[6]

During deposition the vacuum in the growth chamber was always in the low 10^{-10} Torr range. All depositions were carried out with the sample substrate held at room temperature ($T = 300$ K). The deposition rates were measured using a Mathis quartz-crystal thickness monitor. The thicknesses determined independently from RHEED oscillations and the thickness monitor agreed to within $\pm\frac{1}{8}$ monolayers (ML).

The decreases in intensities of dominant XPS and AES peaks of the substrate material during deposition were used to evaluate the overall homogeneity of deposited films. For the Fe and Ag samples the thicknesses determined from AES and/or XPS were in agreement to within $\frac{1}{2}$ ML with those given by the thickness monitor. In addition, the AES and XPS spectra showed that the bulk Ag(001) substrates and epitaxially grown Fe and Ni films were free of surface contaminants (less than 0.05%).

Fe overlayers can be grown epitaxially on bulk Ag substrates. However, it should be pointed out that Ag(001) and Fe(001) lattices are well matched only in the (001) plane. There is an appreciable vertical mismatch due to the large tetragonal distortion between the fcc and bcc lattices. The presence of atomic steps affects the growth and magnetic properties of Fe on the bulk Ag(001). The Fe films epitaxially grown on vicinal Ag substrates[15] showed RHEED oscillations only after three to four atomic layers were deposited, see Fig. 2. Perhaps the complete bcc unit cell has to be formed before a well-defined layer-by-layer growth is attained. This is the healing distance for covering atomic steps. The role of atomic steps is significantly decreased in the epitaxial growth of Fe on Ag(001) thin films deposited on (001) facets of Fe whiskers.[4] Fe whisker facets are almost perfect surfaces with a very low density of atomic steps. RHEED oscillations are visible during the entire growth including the formation of the first atomic layer. Furthermore, the resulting Fe ultrathin films showed a higher perpendicular uniaxial magnetic anisotropy field than Fe films grown on bulk Ag(001) substrates which are accom-

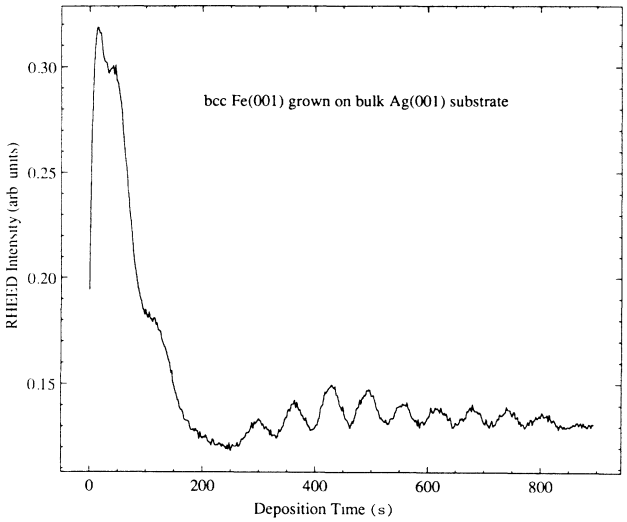

FIG. 2. Oscillations in the intensity of the spectral spot during the growth of Fe on a bulk vicinal Ag(001) substrate. The electron beam angle of incidence was 4° and was rotated 6° azimuthally from the Fe[110] azimuth to avoid interference with Kikuchi lines. After an initial transient period there are regular oscillations whose period corresponds to the deposition of bcc Fe layers.

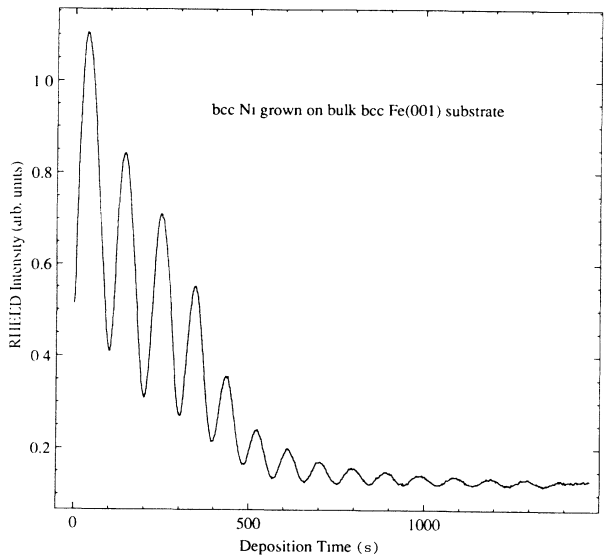

FIG. 4. RHEED oscillations during the growth of Ni on bulk Fe(001). The electron beam angle of incidence was 1° with the sample rotated 6° azimuthally from the [110] direction. In this growth the amplitude of oscillations decays rapidly after the third layer.

panied by numerous steps and relatively short terraces. The sample consisting of [30 ML Au(001)]/[3 ML Fe(001)]/[12 ML Ag(001)]/[Fe(001) whisker facet] exhibited a negative value of the effective in-plane saturation magnetization, $4\pi M_{\text{eff}} = -2.4$ kOe, at room temperature. very recent epitaxial growths of Fe films on bulk singular substrates also exhibited RHEED oscillations during the entire growth, see Fig. 3. Furthermore, films grown on singular Ag substrates indicate that the perpendicular surface anisotropy decreases less with decreasing Fe thickness[12] than on Fe films grown on vicinal Ag substrates.[3]

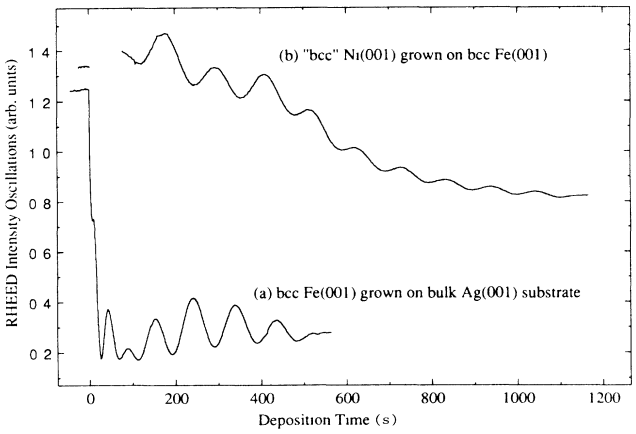

FIG. 3. RHEED oscillations during the growth of (a) Fe on singular Ag(001) and (b) Ni on the Fe overlayer of (a). Notice that the oscillations are present during the entire growths of both layers [data recording failed during first half monolayer in (b)]. The angle of incidence of the electron beam was 0.9°, corresponding to the first anti-Bragg condition, and was directed along the Fe[100] direction.

Ni overlayers epitaxially grown on bulk singular Fe(001) substrates displayed remarkable RHEED oscillations (see Fig. 4). RHEED symmetries and streak separations (hence lattice spacings) of 3–6-ML-thick overlayers are identical with those of the Fe substrate. LEED studies by Wang *et al.*[16] showed that these Ni overlayers indeed have an identical structure to bcc Fe, including the same interlayer relaxation. As the Ni thickness is increased above a critical thickness (3–6 ML, depending on the details of sample preparation) the Ni RHEED pattern along the [110] azimuth starts to develop $c(2\times2)$ diffraction features which strengthen during further growth. However, the main bcc RHEED features remain throughout the rest of the growth. At the onset of the $c(2\times2)$ structure, the amplitude of the RHEED oscillations decreases substantially as shown in Fig. 4, but the film remains homogeneous as determined by XPS and AES. The reconstructed Ni is more complex than that corresponding to the pure $c(2\times2)$ structure. Particularly noticeable are superlattice streaks observable when the RHEED electron beam is directed off the main azimuths.

While neither RHEED nor LEED patterns of reconstructed Ni have been completely understood, RHEED and reflection electron-energy-loss fine structure[5] (REELFS) studies are consistent with the following picture. The first Ni atomic layer is formed by filling the strongly attractive potential wells of the four-fold hollow sites of the Fe(001) atomic plane. Ni atoms of the next Ni ML again fill the fourfold hollow sites [see Fig. 5(a)]. The Ni atoms which are trapped by these attractive potential sites adjust the interplanar distance to accommodate the Ni atomic size. bcc Fe and fcc Ni have almost identical atomic densities and hence nearest-neighbor

spacings. It is therefore not surprising that Ni overlayers grow epitaxially on Fe(001) substrates in the pure bcc structure with the Fe lattice spacing. Structural modifications occurring after the bcc Ni overlayer reaches a critical thickness suggest that the minimum-energy atomic spacing of the metastable structure does not match exactly the Fe substrate spacing. Ni lattice reconstruction is accompanied by a decrease of approximately 2% in RHEED streak separation and a 3–5% decrease in the period of RHEED oscillations which both indicate an ~2% increase in the in-plane lattice spacing. These facts imply that unstrained bcc Ni is 2% mismatched with respect to bcc Fe. The elastic energy stored in the initial strained bcc structure is eventually released by the formation of misfit dislocations and lattice relaxation. Since the facets of the bcc primitive unit cell are formed by {110} planes, the misfit dislocations likely run along these planes. Therefore, the dislocation network orients either along the [100] direction if the {110} dislocation plane is oriented at 45° to the surface normal, or in the [110] direction if the {110} dislocation plane is oriented perpendicular to the surface normal. However, a word of caution is in order. The lattice mismatch is small and should have resulted in a critical thickness of $\sim\frac{1}{2}a/\Delta a = 25$ ML, based on the theory of homogeneous strains;[17] this is appreciably thicker than the values observed. We believe it is likely that the presence of atomic steps during growth triggers the lattice reconstruction at a reduced thickness relative to that expected from homogeneous strains.

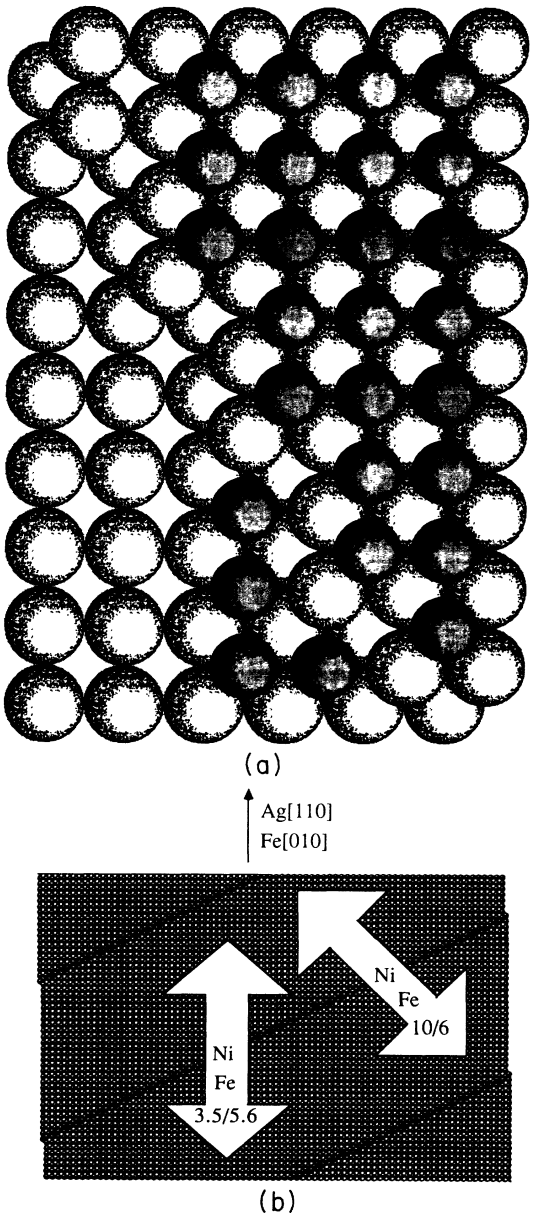

FIG. 5. (a) A detailed top view of the Ag(3 1 100) vicinal surface (large balls) covered by Fe atoms (small balls). The kinked atomic steps are oriented along the [120] Fe direction. Note that the Fe stacking along the surface steps is imperfect due to the large Ag atoms. (b) An idealized global view of the Ag(3 1 100) vicinal surface (each square represents an atom). The vicinal surface can be described as a descending staircase of atomic terraces. The arrows indicate the direction of locked in-plane uniaxial easy axis of reconstructed Ni/Fe(10/6) and unreconstructed Ni/Fe(3.5/5.6) bilayers. The orientation of the axes with respect to the theoretical description is shown in Fig. 6.

The growth of Ni on ultrathin Fe(001) on bulk Ag(001) was similar to the growth of Ni on bulk Fe(001). Both types of Ni films exhibited identical RHEED patterns with the same critical thicknesses. The Ni growth on ultrathin Fe films showed very weak RHEED oscillations when vicinal Ag substrates were used. However the Ni growth on ultrathin Fe on singular Ag substrates showed well-defined RHEED oscillations during the entire growth, see Fig. 3., indicating that the growth of Ni overlayers proceeded layer by layer.

Further information about the Ni/Fe bilayer structure was obtained from careful measurements of the Ag *MNN* (356 eV) and Fe *LMM* (703 eV) Auger peak intensities as a function of Fe and Ni overlayer thicknesses. Agreement of the thicknesses determined from the Ag Auger peak intensity, quartz thickness monitor, and RHEED intensity oscillation showed that the Fe forms a homogeneous layer on Ag. However, all reconstructed Ni overlayers grown on ultrathin Fe films showed an apparent Ni thickness, as determined from the Ag Auger peak intensity, significantly smaller than thicknesses from RHEED intensity oscillations and the quartz thickness monitor. The Ni thicknesses determined from the Fe Auger peak intensities were in excellent agreement with RHEED oscillations and the quartz-thickness-monitor measurements. Therefore the Ni covers the Fe homogeneously. These seemingly contradictory results can be explained by assuming that either the Ag substrate became somewhat exposed along misfit dislocations or that Ag substrate atoms partly diffused along misfit dislocations to the sample surface. In either case the misfit would not be limited to the Ni overlayers but would propagate throughout the whole Ni/Fe bilayer structure. Since the Fe Auger peak intensities in Ni/bulk Fe sandwiches showed a simple exponential decrease with increasing Ni overlayer thicknesses,[6] it can be argued that the network of misfit dislocations caused an in-

creased diffusion of Ag substrate atoms to the surface. Further studies using angularly resolved Auger and XPS measurements are needed to determine the behavior of Ag substrate atoms during bcc Ni lattice reconstruction. A model of the reconstructed Ni overlayer, based on a textbook picture of a relaxed bcc Ni lattice accompanied by a network of misfit dislocations, is perhaps only partly true. Other surface-science tools, such as scanning-tunneling microscopy, are needed to develop a more precise picture of the reconstructed Ni overlayer.

The structural features described above explain why we think of our bcc Ni as "bcc Ni." Very thin Ni layers are indeed epitaxially grown in the pure bcc structure with the lattice spacing corresponding to pure bcc Fe (see Fig. 1). After reaching a critical thickness this simple structure is modified by an array of misfit dislocations and lattice reconstructions.

bcc Ni overlayers can be epitaxially grown directly on Ag(001) substrates. When Ni was deposited on bulk Ag the large vertical mismatch between the Ag and Ni lattices resulted in a more three-dimensional growth. Also, additional superlattice RHEED streaks appeared with increasing Ni overlayer thickness. These additional features were not observed in Ni growths on Fe substrates.

To study the magnetic properties of Ni overlayers in their pure- and reconstructed-bcc forms, several bilayers and one single Ni layer were epitaxially grown.

Sample Ni/Fe(10.5/3.5): [15 ML Au(001)]/[10.5 ML Ni(001)]/[3.5 ML Fe(001)]/[Ag(001) substrate].

Sample Ni/Fe(10/6): [15 ML Au(001)]/[10 ML Ni(001)]/[6 ML Fe(001)]/[Ag(001) substrate].

Sample Ni/Fe(3.5/5.6): [15 ML Au(001)]/[3.5 ML Ni(001)]/[5.6 ML Fe(001)]/[Ag(001) substrate].

Sample Ni/Fe(10): [15 ML Au(001)]/[10 ML Ni(001)]/Ag(001) substrate].

All the above samples were grown on the same vicinal Ag substrate. A detailed inspection of Laue patterns revealed that its surface was oriented very close to the (3 1 100) atomic planes, corresponding to an average misorientation of 1.8°. According to the Van Hove and Somorjai[18] microfacet notation, such a vicinal surface can be viewed as a descending staircase described by kinked atomic steps along the [310] fcc direction ([210] bcc direction) with 50 atoms in the microfacet (001) terrace cell (see Fig. 5).

Since we found that the density of atomic steps played an important role in magnetic properties of ultrathin Fe layers an additional sample was grown on a singular Ag substrate ($<\frac{1}{4}°$ misorientation).

Sample Ni/Fe(9.4/5.7): [15 ML Au(001)]/[9.4 ML Ni(001)]/[5.7 ML Fe(001)]/[singular Ag(001) substrate].

This substrate came from a recently obtained boule with a much smaller mosaic spread (only single spots were visible in the Laue photos). The RHEED patterns showed well-defined diffraction spots that traced the Ewald sphere indicating long-range lattice coherence.

III. EIGENMODES OF ULTRATHIN BILAYERS

Magnetic ultrathin bilayers and superlattices with a strong interface exchange coupling were recently addressed in several papers.[19,20] Rather than solving the problem in terms of general susceptibilities, we have chosen to identify a simple set of variables which describe the overall magnetic properties as functions of single-layer magnetic properties. In our calculations, the strength of the exchange interaction was varied to explore and identify future interesting experiments.

In this section the magnetizations within the individual layers are assumed to be uniform (infinite interatomic exchange) and only the strength of interlayer exchange coupling is allowed to vary. This assumption converts our simplified treatment into the well-known model of exchange-coupled sublattices.[21] All properties of exchange-coupled sublattices are directly applicable to our case. There are two resonance modes in this model: first, the low-frequency acoustic mode in which all magnetizations are parallel, and second, the optical mode in which the magnetizations of the two layers are not parallel. Optical modes occur at higher resonance frequencies due to the presence of the interface exchange field. One should note that the optical mode is observable only if individual layers have different resonant frequencies.

The coordinate system appropriate for our model is shown in Fig. 6. The static magnetizations $\mathbf{M}_s^A$ and $\mathbf{M}_s^B$ lie in the plane of the surface at or near the direction of the applied static in-plane magnetic field ($\hat{\mathbf{y}}$ direction). Incident microwave radiation stimulates transverse rf components of the magnetization $\mathbf{m}^A = m_x^A \mathbf{x} + m_z^A \hat{\mathbf{z}}$ and $\mathbf{m}^B = m_x^B \hat{\mathbf{x}} + m_z^B \hat{\mathbf{z}}$. The response of the magnetic system to the applied fields is found by analyzing the Landau-Lifshitz equation of motion (LL equation) with appropriate boundary conditions. The LL equation for layer A is

$$-\frac{1}{\gamma^A}\frac{\partial \mathbf{M}^A}{\partial t} = \mathbf{M}^A \times \mathbf{H}_{\text{eff}}^A , \tag{1}$$

where γ^A is the gyromagnetic ratio, $\mathbf{M}^A = \mathbf{M}_s^A + \mathbf{m}^A$ is the total magnetization vector, and $\mathbf{H}_{\text{eff}}^A$ is the effective

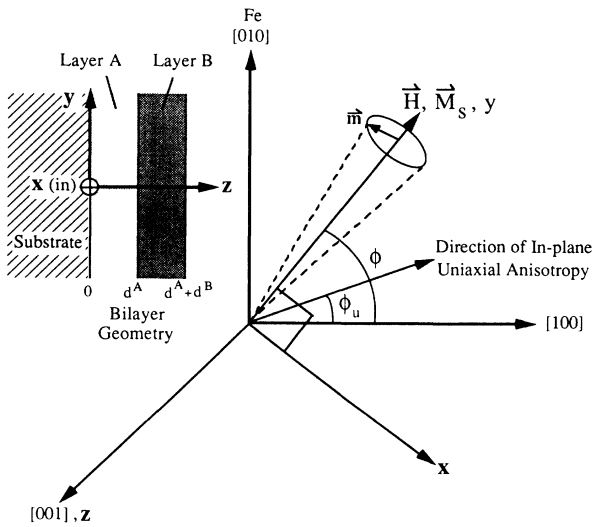

FIG. 6. Coordinate system used for the theory of eigenmodes of bilayers (Sec. III). Angles are measured positive *clockwise* from the [100] direction and therefore the angles ϕ and ϕ_u shown in the figure are negative.

field within the layer A given symbolically by

$$\mathbf{H}_{\text{eff}}^{A}=H\hat{\mathbf{y}}+(\mathbf{H}_{D}^{A})_{\text{eff}}+\mathbf{H}_{K1}^{A}+\mathbf{H}_{Ku}^{A}+\mathbf{H}_{G}^{A}+\mathbf{H}_{\text{ex}}^{A}+h\hat{\mathbf{x}} \ . \quad (2)$$

The equations for layer B are found by replacing all superscripts A by B. H is the externally applied static field and h is the rf field with time dependence $\sim \exp(i\omega t)$. $\mathbf{H}_{K_1}^{A}, \mathbf{H}_{K_u}^{A}$ are anisotropy fields which are defined by the energy expressions for cubic and in-plane uniaxial anisotropies:

$$E_{\text{cubic}}=K_1^{A}(\alpha_1^2\alpha_2^2+\alpha_1^2\alpha_3^2+\alpha_2^2\alpha_3^2) \ , \quad (3)$$

$$E_u=-K_u^{A}\left[\frac{\mathbf{M}^{A}\cdot\mathbf{n}}{M_s^{A}}\right]^2 , \quad (4)$$

where $\mathbf{n}$ is a unit vector along the in-plane uniaxial axis. The damping field is given by

$$\mathbf{H}_{G}^{A}=-\frac{G^{A}}{(\gamma^{A}M_s^{A})^2}\frac{\partial\mathbf{M}^{A}}{\partial t} \ ,$$

where G^{A} is the Gilbert damping parameter. The exchange field is given by $\mathbf{H}_{\text{ex}}^{A}=[2A^{A}/(M_s^{A})^2]\nabla^2\mathbf{m}$, where A^{A} is the exchange-coupling coefficient (ergs/cm). The effective demagnetizing field, $(\mathbf{H}_{D}^{A})_{\text{eff}}$, will be discussed later in this section.

It is useful to take explicitly into account that the experiments are sensitive to the integrated magnetization in the slab. Define

$$\mathcal{M}_{\alpha}^{A}=\int_{0}^{d^{A}} m_{\alpha}^{A}\,dz, \quad \mathcal{M}_{\alpha}^{B}=\int_{d^{A}}^{d^{A}+d^{B}} m_{\alpha}^{B}\,dz \ .$$

where $\alpha=x$ or z and d^{A} and d^{B} are the slab thicknesses.

The following equations of motion are obtained from Eqs. (1) and (2) by using the time dependence $\sim \exp(i\omega t)$, and integrating across the slab:

$$-i\frac{\omega}{\gamma^{A}}\mathcal{M}_x^{A}+\left[B_{\text{eff}}^{A}+\frac{K_1^{A}}{2M_s^{A}}[3+\cos(4\varphi)]+\frac{K_u^{A}}{M_s^{A}}\{1+\cos[2(\varphi-\varphi_u)]\}+i\frac{G^{A}}{\gamma^{A}M_s^{A}}\frac{\omega}{\gamma^{A}}\right]\mathcal{M}_z^{A}=2\frac{A^{A}}{M_s^{A}}\frac{\partial m_z^{A}}{\partial z}\bigg|_{z=d^{A}} , \quad (5a)$$

$$\left[H+\frac{2K_1^{A}}{M_s^{A}}\cos(4\varphi)+\frac{2K_u^{A}}{M_s^{A}}\cos[2(\varphi-\varphi_u)]+i\frac{G^{A}}{\gamma^{A}M_s^{A}}\frac{\omega}{\gamma^{A}}\right]\mathcal{M}_x^{A}+i\frac{\omega}{\gamma^{A}}\mathcal{M}_z^{A}=M_s^{A}h^{A}d^{A}+2\frac{A^{A}}{M_s^{A}}\frac{\partial m_x^{A}}{\partial z}\bigg|_{z=d^{A}} . \quad (5b)$$

A similar pair of equations can be written for the second layer (layer B); they can be obtained from Eq. (5) by replacing the superscript A by B, and by changing the sign in front of the derivative terms (because the derivative must be evaluated at the interface which is the rear surface for slab A but the front surface for slab B). Note that the magnetization derivatives at the front of layer A, and at the rear of layer B, have been set equal to zero. In the very-thin-film limit, which is of interest here, surface pinning terms behave like uniaxial anisotropies which are inversely proportional to the thickness.[13] In the present instance, a surface energy having a uniaxial axis perpendicular to the surface has been incorporated into the equations of motion through an effective demagnetizing field[3]

$$B_{\text{eff}}^{A}=H+(\mathbf{H}_{D}^{A})_{\text{eff}}=H+(4\pi D_{\perp}M_s^{A})_{\text{eff}} \ ,$$

where

$$(4\pi D_{\perp}M_s^{A})_{\text{eff}}=4\pi D_{\perp}M_s^{A}+\frac{2K_s^{A}}{d^{A}M_s^{A}} \ ,$$

and $D_{\perp}$ is the demagnetizing factor for an ultrathin layer (see the Appendix).

The derivatives in the equations of motion, (5a) and (5b), can be evaluated from the torque equations which describe the motion of the spins at the interface between the A and the B layers. We have used a pair interaction energy of the form $E=-2J\mathbf{S}_i\cdot\mathbf{S}_j$ where $\mathbf{S}_i$ and $\mathbf{S}_j$ are nearest neighbors and J is the exchange integral. In a bcc cubic material J is related to the exchange stiffness parameter, A, through

$$J=\frac{aA}{2S^2} \ ,$$

where a is the side of a bcc elementary cube cell and the volume per atom is $a^3/2$.

Interface spins have been assumed to couple through a pair interaction characterized by J^{AB}: to preserve the continuity of notation we have defined an interface exchange stiffness parameter $A^{AB}\equiv 2J^{AB}S^{A}S^{B}/a^{AB}$ where $a^{AB}\equiv(a^{A}a^{B})^{1/2}$. a^{A} and a^{B} are the bcc lattice spacings for layers A and B, respectively. A^{AB} can be estimated from the bulk values for Fe and Ni.

For layers of bcc material having four nearest neighbors, the effective fields acting on an interface spin are given by

$$\mathbf{H}^{AA}=-\frac{4A^{A}}{(M_s^{A})^2}\frac{1}{a^{A}}\left[\frac{\partial\mathbf{m}^{A}}{\partial z}\right]\bigg|_{z=d^{A}} ,$$

$$\mathbf{H}^{AB}=\frac{8A^{AB}}{M_s^{A}M_s^{B}}\frac{a^{AB}}{(a^{A})^3}\mathbf{M}^{B} \ ,$$

$$\mathbf{H}^{BA}=\frac{8a^{AB}}{M_s^{A}M_s^{B}}\frac{a^{AB}}{(a^{B})^3}\mathbf{M}^{A} \ ,$$

$$\mathbf{H}^{BB}=\frac{4A^{B}}{(M_s^{B})^2}\frac{1}{a^{B}}\left[\frac{\partial\mathbf{m}^{B}}{\partial z}\right]\bigg|_{z=d^{A}} .$$

$\mathbf{H}^{\beta\alpha}$ is the effective field acting on a β-layer surface spin due to nearest neighbors in an α layer.

The above effective fields can now be used to write the Landau-Lifshitz equations of motion for the magnetizations $\mathbf{m}^{A}, \mathbf{m}^{B}$ at the interface between layers A and B. In these equations all fields other than the exchange fields

are negligible. This procedure results in the Hoffman boundary conditions:

$$\left.\frac{2A^A}{M_s^A}\frac{\partial m_x^A}{\partial z}\right|_{z=d^A}=8A^{AB}\frac{a^{AB}}{(a^A)^2}\left[\frac{1}{d^B}\left[\frac{\mathcal{M}_x^B}{M_s^B}\right]-\frac{1}{d^A}\left[\frac{\mathcal{M}_x^A}{M_s^A}\right]\right], \tag{6}$$

$$\left.\frac{2A^A}{M_s^A}\frac{\partial m_z^A}{\partial z}\right|_{z=d^A}=8A^{AB}\frac{a^{AB}}{(a^A)^2}\left[\frac{1}{d^B}\left[\frac{\mathcal{M}_z^B}{M_s^B}\right]-\frac{1}{d^A}\left[\frac{\mathcal{M}_z^A}{M_s^A}\right]\right],$$

plus two equivalent equations for $(\partial m_x^B/\partial z)|_{d^A}$ and $(\partial m_z^B/\partial z)|_{d^A}$.

The 4×4 system of equations which results from the elimination of the derivative terms from Eqs. (5) using Eq. (6) (and their analogues for layer B) can be solved by straightforward matrix algebra. The numerator and denominator of the effective susceptibility $[\chi=(\mathcal{M}_x^A+\mathcal{M}_x^B)/h_x]$ are quadratic polynomials in the interface coupling A^{AB}. A general expression for the susceptibility χ is extremely long and impractical. However, for strong interlayer exchange coupling, only the quartic term in ω and the quadratic terms in A^{AB} are important. The resulting expression for the resonance condition simplifies significantly and can be interpreted in terms of a high-frequency optical mode and a low-frequency acoustic mode. The low-frequency resonance is given by the root of the coefficient of the $(A^{AB})^2$ term. Using a computer-aided algebraic evaluation of the denominator results in the following equation:

$$\frac{\mu^A N^A}{\mu^B N^B}\left[A_1^A A_2^A-\left[\frac{\omega}{\gamma^A}\right]^2\right]+\frac{\mu^B N^B}{\mu^A N^A}\left[A_1^B A_2^B-\left[\frac{\omega}{\gamma^B}\right]^2\right]+\left[A_1^A A_2^B+A_2^A A_1^B-2\left[\frac{\omega}{\gamma^A}\frac{\omega}{\gamma^B}\right]\right]=0\,, \tag{7}$$

where

$$A_1^A=B_{\text{eff}}^A+\frac{K_1^A}{2M_s^A}[3+\cos(4\varphi)]+\frac{K_u^A}{M_s^A}\{1+\cos[2(\varphi-\varphi_u)]\}+i\frac{G^A}{\gamma^A M_s^A}\frac{\omega}{\gamma^A}\,,$$

$$A_2^A=H+\frac{2K_1^A}{M_s^A}\cos(4\varphi)+\frac{2K_u^A}{M_s^A}\cos[2(\varphi-\varphi_u)]+i\frac{G^A}{\gamma^A M_s^A}\frac{\omega}{\gamma^A}\,,$$

and A_1^B and A_2^B are found by replacing the superscripts A by B in the above equations. N^A, N^B are the number of monolayers for A and B, and $\mu^A=M_s^A(a^A)^3/2$ and $\mu^B=M_s^B(a^B)^3/2$ are the magnetic moments per atom.

Equation (7) can be further rewritten as

$$\omega^2\left[\frac{\mu^A N^A}{\gamma^A}+\frac{\mu^B N^B}{\gamma^B}\right]^2-(\mu^A N^A A_2^A+\mu^B N^B A_2^B)(\mu^A N^A A_1^A+\mu^B N^B A_1^B)=0\,.$$

Dividing this equation by $(\mu^A N^A+\mu^B N^B)^2$ leads to

$$\omega^2\left[\frac{\mu^A N^A}{\gamma^A(\mu^A N^A+\mu^B N^B)}+\frac{\mu^B N^B}{\gamma^B(\mu^A N^A+\mu^B N^B)}\right]^2-\left[\frac{\mu^A N^A A_2^A}{(\mu^A N^A+\mu^B N^B)}+\frac{\mu^B N^B A_2^B}{(\mu^A N^A+\mu^B N^B)}\right]\left[\frac{\mu^A N^A A_1^A}{(\mu^A N^A+\mu^B N^B)}+\frac{\mu^B N^B A_1^B}{(\mu^A N^A+\mu^B N^B)}\right]=0\,.$$

Introducing the bilayer scaling parameter α given by

$$\alpha=\frac{\mu^A N^A}{[\mu^A N^A+\mu^B N^B]}=\frac{M_s^A N^A(a^A)^3/2}{[M_s^A N^A(a^A)^3/2+M_s^B N^B(a^B)^3/2]} \tag{8}$$

the low-frequency condition can be written in its final form:

$$\omega^2\left[\frac{\alpha}{\gamma^A}+\frac{(1-\alpha)}{\gamma^B}\right]^2-[\alpha A_2^A+(1-\alpha)A_2^B][\alpha A_1^A+(1-\alpha)A_1^B]=0\,. \tag{9}$$

The comparison of Eq. (9) with an effective single-layer resonance condition given by

$$(\omega/\gamma)^2=(B_{\text{eff}}+\tfrac{1}{4}H_{K_1}[3+\cos(4\varphi)]+\tfrac{1}{2}H_{K_u}\{1+\cos[2(\varphi-\varphi_u)]\}+i\,\Delta H)\times\{H+H_{K_1}\cos(4\varphi)+H_{K_u}\cos[2(\varphi-\varphi_u)]+i\,\Delta H\} \tag{10}$$

leads to the scaling laws for effective fields of strongly exchange-coupled bilayers:

$$
\begin{aligned}
H_{K_1} &= \alpha \frac{2K_1^A}{M_s^A} + (1-\alpha)\frac{2K_1^B}{M_s^B} , \\
H_{K_u} &= \alpha \frac{2K_u^A}{M_s^A} + (1-\alpha)\frac{2K_u^B}{M_s^B} , \\
\frac{\omega}{\gamma} &= \alpha \frac{\omega}{\gamma^A} + (1-\alpha)\frac{\omega}{\gamma^B} , \\
\Delta H &= \alpha \frac{\omega G^A}{(\gamma^A)^2 M_s^A} + (1-\alpha)\frac{\omega G^B}{(\gamma^B)^2 M_s^B} , \\
(4\pi D_\perp M_s)_{\text{eff}} &= \alpha (4\pi D_\perp M_s^A)_{\text{eff}} + (1-\alpha)(4\pi D_\perp M_s^B)_{\text{eff}} .
\end{aligned}
\tag{11}
$$

All expressions in Eqs. (11) are effective fields and hence the effective fields of individual layers form the set of natural variables of magnetic bilayers. The general scaling law can therefore be written in the form

$$
H_{\text{eff}}^{\text{bilayer}} = \alpha H_{\text{eff}}^A + (1-\alpha) H_{\text{eff}}^B . \tag{12}
$$

Equation (12) can be used recursively with Eq. (10) to form a generalized expression for the effective field associated with a multilayer structure:

$$
H_{\text{eff}}^{\text{multilayer}} = \sum_i \alpha^i H_{\text{eff}}^i , \tag{13}
$$

where

$$
\alpha^i = \mu^i N^i \Big/ \sum_j \mu^j N^j .
$$

The bilayer magnetic response for small and intermediate values of A^{AB} is more complex and can be investigated only by computer calculations. In the limit $A^{AB}=0$, the layers A and B behave independently in FMR measurements. In BLS studies of the optical-mode resonance, they are still coupled by the rf demagnetizing fields which are a consequence of an in-plane spatial dependence of the magnetization.[22,23]

Calculations were carried out to demonstrate the role of variable interface exchange coupling on the bilayer magnetic response. We chose a bilayer composed of a 10-ML Fe layer weakly coupled to a 6-ML Fe layer. These layers act as two distinct magnetic materials with different resonant frequencies because of the $1/d$ dependence of the perpendicular uniaxial anisotropy. For an arbitrary value of A^{AB} the rf susceptibility denominator leads to two resonance modes. The modes can be described either by fixing the field and scanning the frequency (BLS), or by fixing the frequency and scanning the field (FMR). The character of the modes in the BLS picture is shown in Fig. 7. As A^{AB} is increased from zero, the lower branch reaches a fixed frequency given by Eq. (11). The upper branch is almost linear with A^{AB} and will be called the soft optical mode. Since BLS measurements can be extended to 500 GHz, one can study the interlayer exchange up to a value of 1×10^{-7} ergs/cm which is a significant portion of the bulk exchange ($\sim10^{-6}$ ergs/cm).

Figure 8 illustrates the FMR dependence on interlayer exchange (A^{AB}). In contrast to BLS, the FMR optical resonance field shifts downwards to lower dc magnetic fields with increasing A^{AB}.

One should point out that antiferromagnetic coupling ($A^{AB}<0$) would result in reverse trends (see Figs. 7 and 8). Both BLS and FMR can therefore distinguish between ferromagnetic and antiferromagnetic interface exchange coupling.

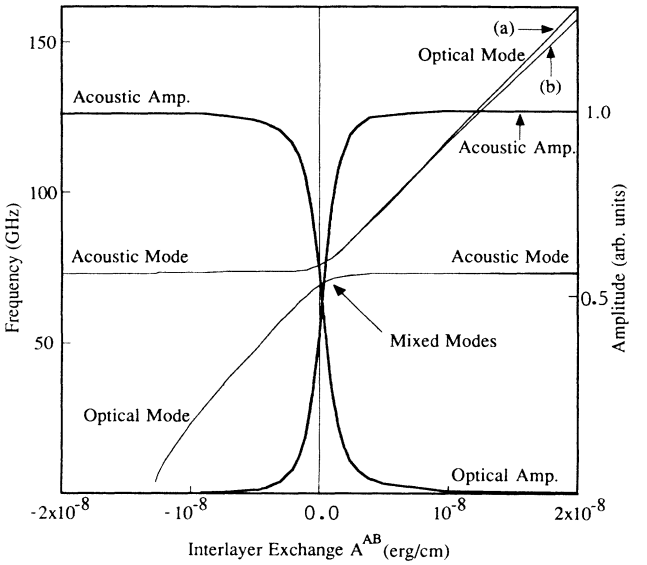

FIG. 7. Calculated resonant frequencies and amplitudes of low-frequency modes in a bilayer composed of a 10-ML-thick Fe layer weakly exchange coupled to a 6-ML-thick layer. The applied field is fixed at 20 kOe. See Fig. 9 caption for the Fe magnetic parameters. Curve (a) is calculated using the simplified theory of Sec. III. Curve (b) and the amplitude curves use the discrete model extended to include demagnetizing and anisotropy fields and Gilbert damping.

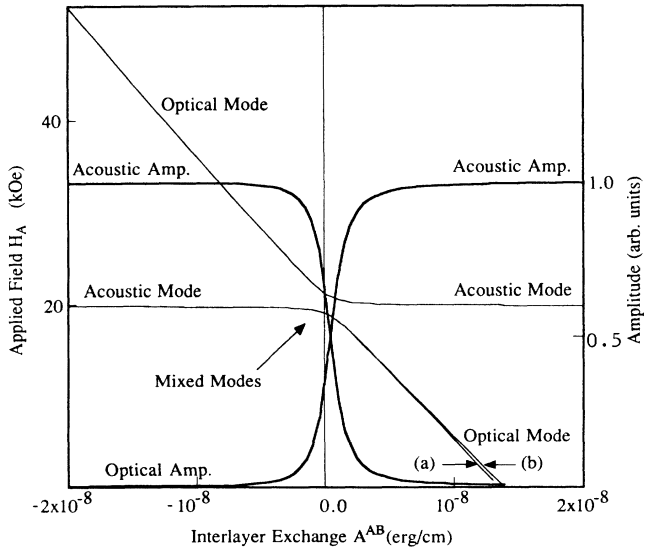

FIG. 8. The curves are calculated as in Fig. 7 but using a fixed frequency of 73 GHz and varying the applied magnetic field.

The above calculations show that BLS and FMR are well suited to the study of small interlayer exchange coupling. FMR is a better technique for investigating the onset of interlayer exchange since BLS is affected by dipolar interactions even in the absence of exchange coupling. Assuming that the interlayer exchange decreases exponentially with a decay length corresponding to the interlayer spacing, spacer layers ~6–8 ML thick could be used to investigate the role of long-range exchange coupling in itinerant ultrathin bilayers which form the building blocks of magnetic superlattices. Such measurements would be complementary to the experimental work on thick magnetic bilayers carried by Grünberg and coworkers[22] and corresponding theoretical work by Cochran and Dutcher[23] for BLS and Vayhinger and Kronmüller[24] for FMR.

In the limit of a strong interface exchange coupling, the soft optical mode becomes the first optical mode of the tightly exchange-coupled atomic layers.

A. The discrete model of exchange-coupled bilayers

The theoretical treatment of optical modes requires further refinement. The simplified model of exchange-coupled magnetic layers discussed above fails completely when the interface exchange becomes comparable to the interplanar exchange. True optical modes should be described by taking the full exchange coupling between all atomic layers into account. Since our MBE studies are carried out on ultrathin ferromagnetic films, a discrete model of exchange-coupled atomic planes can be used without introducing too much computational complexity.

A computer program has been written in which the Landau-Lifshitz equations have been written for nearest-neighbor exchange-coupled atomic planes. Each plane can in principle have different magnetic properties. In-plane anisotropies with fourfold and twofold symmetries, surface anisotropy, Gilbert damping, and demagnetizing fields have been included. The general equations are complicated. For clarity we demonstrate the structure of the equations of motion for a simplified example in which all interactions except the exchange interaction are neglected. This allows us to introduce circularly polarized modes for which the LL equations of motion reduce to the following.

(i) Surface plane of layer A:

$$(\beta^A M_s^A-\omega/\gamma^A)m_+^A(0)-\beta^A M_s^A m_+^A(1)=0\ . \quad (14a)$$

(ii) Bulk planes in layer A (with $2\le I\le S-1$):

$$(2\beta^A M_s^A-\omega/\gamma^A)m_+^A(I)-\beta^A M_s^A m_+^A(I-1)-\beta^A M_s^A m_+^A(I+1)=0\ . \quad (14b)$$

(iii) Planes at the interface between layers A and B:

$$(2\beta^A M_s^A+\beta^{AB}M_s^B-\omega/\gamma^A)m_+^A(S)-\beta^A M_s^A m_+^A(S-1)-\beta^{AB}M_s^A m_+^B(S+1)=0\ , \quad (14c)$$

$$(2\beta^B M_s^B+\beta^{AB}M_s^A-\omega/\gamma^B)m_+^B(S+1)-\beta^B M_s^B m_+^A(S)-\beta^{AB}M_s^A m_+^B(S+1)=0\ .$$

(iv) Bulk planes in layer B (with $S+1\le J\le N-1$):

$$(\beta^B M_s^B-\omega/\gamma^B)m_+^B(J)-\beta^B M_s^B m_+^B(J-1)-\beta^B M_s^B m_+^B(J+1)=0\ . \quad (14d)$$

(v) Surface plane of layer B:

$$(\beta^B M_s^B-\omega/\gamma^B)m_+^B(N-1)-\beta^B M_s^B m_+^B(N)=0\ . \quad (14e)$$

Here $m_+^A(\mathrm{I})=m_x^A(\mathrm{I})+im_y^A(\mathrm{I})$ and $m_+^B(\mathrm{I})=m_x^B(\mathrm{I})+im_y^B(\mathrm{I})$ are right-hand circularly polarized magnetization components of the atomic plane I and

$$\beta^A=\frac{8A^A}{a^2(M_s^A)^2},\quad \beta^B=\frac{8A^B}{a^2(M_s^B)^2},\quad \beta^{AB}=\frac{8A^{AB}}{a^2M_s^AM_s^B}\ .$$

We have assumed, for simplicity, that $a^A=a^B=a$.

As mentioned above, the first optical resonance corresponds to the soft optical mode in the limit of strong interfacial exchange coupling. The calculations shown in Fig. 9 were carried out for a 6-ML Fe layer and a (10 ML Ni)/(6 ML Fe) bilayer having a strong interfacial exchange coupling ($A^{AB}=1.5\times10^{-6}$ ergs/cm). The resonance modes are in the range of Raman light scattering (RLS) experiments and there are as many modes as there

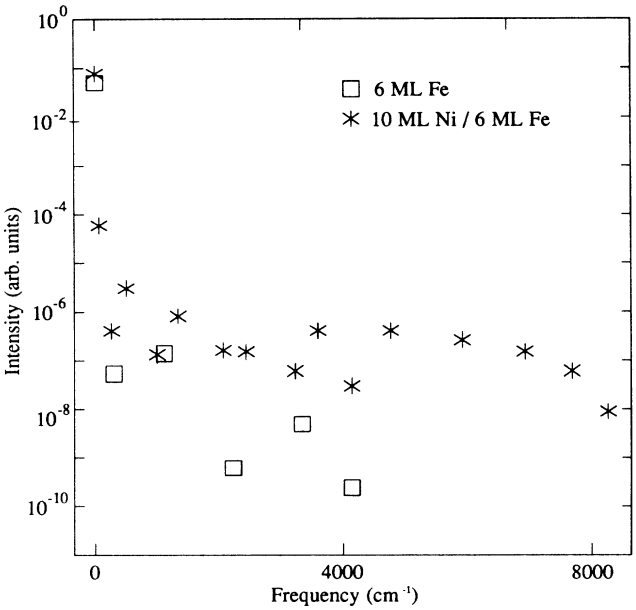

FIG. 9. Intensity of optical modes vs frequency (cm^{-1}) for a 6-ML-Fe single layer and a (10 ML Ni/6 ML Fe) bilayer. The parameters of the Fe are $4\pi M_s=21.55$ kG, a g factor of 2.09, a Gilbert damping parameter of 1×10^8 sec^{-1}, $K_1=4.8\times10^5$ ergs/cm^3, and the exchange coefficient $A=2.0\times10^{-6}$ ergs/cm. The parameters of the Ni are $4\pi M_s=6.14$ kG, a g factor of 2.21, a Gilbert damping parameter of 3×10^9 sec^{-1}, $K_1=8.5\times10^5$ ergs/cm^3, and the exchange coefficient $A=1.0\times10^{-6}$ ergs/cm. The coupling exchange was 1.5×10^{-6} and the applied field was 20 kOe. The 6 ML Fe has surface pinning $K_s=0.7$ ergs/cm^2 on one surface and 0.5 ergs/cm^2 on the other. This models an Fe layer grown on Ag and covered by a Au overlayer (Ref. 25). A value $K_s=0.5$ ergs/cm^2 was used for the Fe in the bilayer.

are atomic planes. In Fig. 9 we have plotted the integral of the optical response for each mode as a function of the mode frequency. The optical response is defined as the sum over all atomic planes of the area under the peak of the transverse magnetization (m_x) versus frequency assuming a uniform driving field. Note that optical modes of single magnetic layers pinned equally on both surfaces have zero intensity because they do not couple to a homogeneous driving field. Different values of surface pinning on the interfaces or different magnetic parameters of the layers of a bilayer break the symmetry of the system and couple the optical modes to a homogeneous driving field. For the above parameters the calculated intensities of the optical modes are weak (see Fig. 9); a very high sensitivity would be required to observe them. A search for optical modes in Ni/Fe bilayers using RLS is in progress.

IV. EXPERIMENTAL RESULTS AND ANALYSIS

To determine $4\pi M_{\text{eff}}$, H_{K_1}, H_{K_u}, and the g factor we carried out FMR measurements at 9.5, 24.0, 36.6, and 73.0 GHz. The samples were used as the end plates of TE_{01N} cylindrical cavities (doughnut mode) which gave constant sensitivity independent of the orientation of the magnetic field in the plane of the specimen. The dc magnetic field was rotated in the sample plane over the full 360° to measure the in-plane anisotropies. We used standard lock-in amplifier detection techniques with 127 Hz field modulation to detect the signal and 60 kHz repeller modulation to stabilize the frequency of the klystron to the cavity containing the sample. FMR sensitivity was excellent. FMR lines as wide as 1000 Oe were readily detectable in samples 2–3 ML thick. FMR measurements were carried out at room and liquid-nitrogen (LN_2) temperatures.

BLS measurements were performed in air at room temperature using a multipassed, tandem (4+2 passes) Fabry Perot interferometer. Typically 100 mW of Ar^+-ion laser light ($\lambda=5145$ Å), polarized in the scattering plane, was focused on the sample surface. 180° backscattered light, polarized perpendicular to the scattering plane, was collected and analyzed in the interferometer. A dc magnetic field, variable between 0 and 10 kOe, was applied in the sample plane and perpendicular to the scattering plane. The samples could be rotated through 360° in the sample plane. High-resolution frequency measurements, ±0.03 GHz, were performed with a single interferometer (four passes) using a free spectral range which was small compared with the mode frequency. This technique has been used to accurately measure the surface-mode frequency of iron whiskers.[26] BLS signals were easily observed for the bilayer films, even when only four passes through a single interferometer were used. The measured surface-mode frequencies for the bilayer films ranged between 10 and 40 GHz for applied fields between 0 and 10 kOe.

The most striking difference between the reconstructed Ni/Fe bilayers and single Fe layers is the presence of a large in-plane anisotropy with fourfold symmetry (hereafter termed "fourfold anisotropy") in the bilayer samples, see Figs. 10, 11 and 12, whereas in ultrathin Fe films the

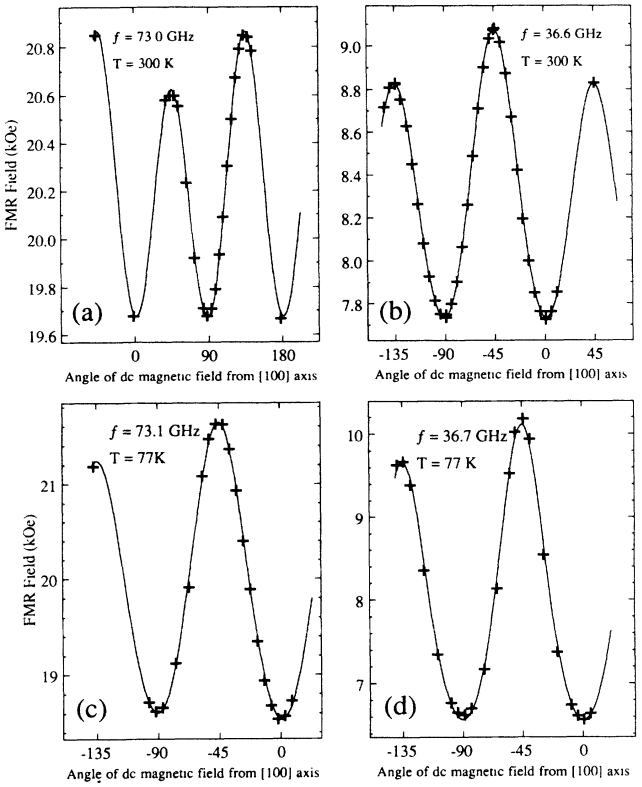

FIG. 10. The in-plane dependences of measured FMR field for the [15 ML Au(001)]/[10 ML Ni(001)]/[6 ML Fe(001)]/bulk Ag(001)] [sample Ni/Fe(10/6)] at room and LN_2 temperatures. Solid lines are calculated angular dependences of the FMR field. Calculations were carried out with magnetic parameters obtained from a multiparameter χ^2 function minimization routine. (a) $f=72.925$ GHz, $H_{K_1}=0.760$ kOe, $H_{K_u}=0.149$ kOe, $\varphi_u=45°$ (along Fe[110], g-factor is 2.1, $(4\pi D_\perp M_s)_{\text{eff}}=9.75$ kG, $T=300$ K. (b) $f=36.62$ GHz, $H_{K_1}=0.789$ kOe, $H_{K_u}=0.143$ kOe, $\varphi_u=45°$ (along Fe[110]), g factor is 2.1, $(4\pi D_\perp M_s)_{\text{eff}}=9.75$ kG, $T=300$ K. (c) $f=72.97$ GHz, $H_{K_1}=2.04$ kOe, $H_{K_u}=-0.253$ kOe, $\varphi_u=41°$, g factor is 2.103, $(4\pi D_\perp M_s)_{\text{eff}}=9.346$ kG, $T=77$ K. (d) $f=36.76$ GHz, $H_{K_1}=2.14$ kOe, $H_{K_u}=-0.257$ kOe, $\varphi_u=41°$, g factor is 2.103, $(4\pi D_\perp M_s)_{\text{eff}}=9.346$ kG, $T=77$ K.

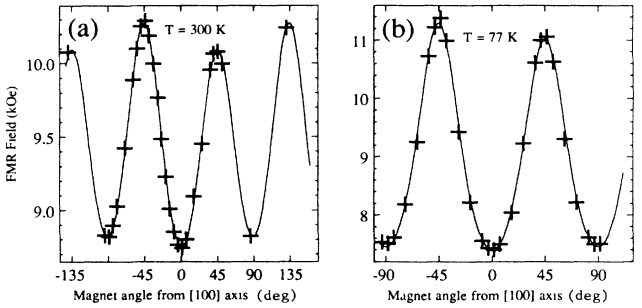

FIG. 11. The in-plane angular dependence of measured FMR field for the [15 ML Au(001)]/[10.5 ML Ni(001)]/[3.5 ML Fe(001)]/[bulk Ag(001)] [sample Ni/Fe(10.5/3.5)]. (a) $f=36.627$ GHz, $H_{K_1}=0.974$ kOe, $H_{K_u}=0.119$ kOe, $\varphi_u=35°$, g factor is 2.149, $(4\pi D_\perp M_s)_{\text{eff}}=5.376$ kG, $T=300$ K. (b) $f=36.71$ GHz, $H_{K_1}=2.57$ kOe, $H_{K_u}=0.164$ kOe, $\varphi_u=38°$, g factor is 2.149, $(4\pi D_\perp M_s)_{\text{eff}}=4.83$ kG, $T=77$ K.

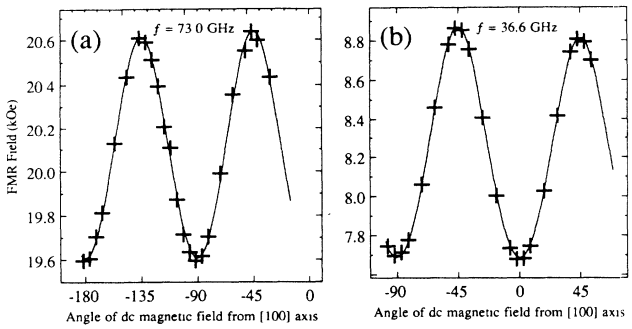

FIG. 12. The in-plane angular dependence of measured FMR field for the [15 ML Au(001)]/[9.4 ML Ni(001)]/[5.7 ML Fe(001)]/[bulk singular Ag(001)] [sample Ni/Fe(9.4/5.6)]. (a) $f=36.61$ GHz, $H_{K_1}=0.749$ kOe, $H_{K_u}=0.033$ kOe, $\varphi_u=0°$ (along Fe[100]), g factor is 2.107, $(4\pi D_\perp M_s)_{\text{eff}}=9.816$ kG, $T=300$ K. (b) $f=73.01$ GHz, $H_{K_1}=0.723$ kOe, $H_{K_u}=0.017$ kOe, $\varphi_u=0°$ (along Fe[001]), g factor is 2.107, $(4\pi D_\perp M_s)_{\text{eff}}=9.816$ kG, $T=300$ K.

fourfold anisotropy is weak. Fe samples less than 3.5 ML thick show no in-plane anisotropies even at LN_2 temperatures; see Table I. The in-plane fourfold anisotropy of the Ni/Fe bilayers can be as large as ~ 6 kOe at LN_2 temperature, appreciably exceeding those observed in bulk Fe. Consequently, the bilayer saturation magnetization, when oriented away from the planar [100] easy axis, lagged behind the in-plane dc magnetic field. The angular dependence of the FMR field is thus not described by simple fourfold and twofold symmetry terms, but exhibits a somewhat smaller curvature around the easy axis and sharper curvature around the [110] hard axis, see Figs. 10–12. Note that there is also a weak in-plane anisotropy with twofold symmetry (hereafter termed "twofold anisotropy") for samples grown on the vicinal substrates (Figs. 10 and 11) which are significantly decreased ($\sim\times 4$) in the bilayer grown on a singular Ag(001) substrate; see Fig. 12.

The fourth-order magnetic anisotropy energy in ultrathin films epitaxially grown in the (001) plane can be described by

$$E_4=-\tfrac{1}{2}K_{1\parallel}(\alpha_x^4+\alpha_y^4)-\tfrac{1}{2}K_{1\perp}\alpha_z^4 , \tag{15}$$

where α_x, α_y, and α_z are the directional cosines of the magnetization vector with respect to the cubic crystalline axes, and $K_{1\parallel}$ and $K_{1\perp}$ describe the strength of the fourth-order anisotropy parallel (fourfold in-plane) and perpendicular to the sample surface, respectively.

This expression can be rewritten in the form

$$E_4=-\tfrac{1}{2}K_{1\parallel}(\alpha_x^4+\alpha_y^4+\alpha_z^4)-\tfrac{1}{2}(K_{1\perp}-K_{1\parallel})\alpha_z^4 . \tag{16}$$

The first part of the expression is equivalent to a regular cubic anisotropy term:

$$E_{\text{cubic}}=K_{1\parallel}(\alpha_x^2\alpha_y^2+\alpha_y^2\alpha_z^2+\alpha_z^2\alpha_x^2) . \tag{17}$$

The remaining part of the fourth-order anisotropy energy corresponds to a fourth-order perpendicular uniaxial energy having its symmetry axis perpendicular to the sample surface. For the saturation magnetization oriented in the plane of the specimen a fourth-order perpendicular uniaxial anisotropy plays no role in FMR and BLS measurements since the corresponding effective field is proportional to the third power of the rf perpendicular magnetization component and is negligible. Therefore, in our

TABLE I. Properties of Ni/Fe bilayers and single Fe overlayers at room and liquid-nitrogen temperatures.

Sample	Temp. (K)	$(4\pi D_\perp M_s)_{\text{eff}}$ (kOe)	g	H_{K_1}[a] (kOe)	H_{K_u}[b] (kOe)	φ_u[c] (deg)	ΔH(36.6 GHz) (kOe) easy	hard
(3.5 ML Ni)/(5.6 ML Fe)	300	8.9	2.09	0.14	−0.044	0	0.230	0.170
(vicinal Ag substrate)	77	9.29	2.09	0.280	−0.050	0	0.200	0.165
(9.4 ML Ni)/(5.7 ML Fe) (singular Ag substrate)	300	9.82	2.107	0.735	0.025	45	0.253	0.525
(10 ML Ni)/(6 ML Fe)	300	9.75	2.1	0.770	0.146	45	0.285	0.611
(vicinal Ag substrate)	77	9.346	2.103	2.090	0.254	41	0.350	1.130
(10.5 ML Ni)/(3.5 ML Fe)	300	5.376	2.149	0.992	0.120	35	0.307	0.757
(vicinal Ag substrate)	77	4.83	2.149	2.570	0.160	38	0.380	1.313
3.5 ML Fe[a]	300	3.5	2.09	0.0	0.0		0.34[e]	
(vicinal Ag substrate)	77	3.84	2.09	0.0	0.0		0.47[e]	
5.6 ML Fe[d]	300	7.7	2.09	0.14	−0.044	0	0.15[e]	
(vicinal Ag substrate)	77	8.7	2.09	0.26	−0.13	0	0.17[e]	
6 ML Fe[d]	300	8.1	2.09	0.16	−0.044	0	0.14[e]	
(vicinal Ag substrate)	77	9.16	2.09	0.29	−0.13	0	0.16[e]	

[a] H_{K_1} is the effective fourfold in-plane anisotropy field defined by $2K_1/M_s$. The values quoted are the averaging of data obtained at 36 and 73 GHz.

[b] H_{K_u} is the effective twofold in-plane anisotropy field defined by $2K_u/M_s$. The values quoted are the averaging of data obtained at 36 and 73 GHz.

[c] Angular direction of the uniaxial anisotropy axis with respect to the in-plane Fe[100] direction.

[d] The parameters for single Fe films were obtained by interpolation from previously measured Fe films of similar thicknesses.

[e] The easy- and hard-axis FMR linewidths were nearly the same and are represented by their average values.

geometry, the full fourth-order anisotropy energy term and the cubic anisotropy term, Eqs. (15) and (17), are indistinguishable.

The angular dependence of the FMR field was analyzed using the full treatment of the cubic and in-plane uniaxial anisotropies. This included the noncollinearity of the saturation magnetization with the in-plane dc magnetic field. Computer fits carried out with MINUIT, a multiparameter χ^2 function minimization routine, are excellent, see Figs. 10–12 and 14, and the results are summarized in Table I.

In addition, BLS measurements of the surface-mode frequency as a function of the in-plane rotation angle were performed for a fixed magnetic field. High-resolution measurements for sample Ni/Fe(10/6), obtained using a single interferometer, are shown in Fig. 13. The BLS spectrum in Fig. 13(a) shows two peaks, one shifted up in frequency and the other shifted down, which belong to different orders of the interferometer. The frequency shift between the two peaks was measured as the in-plane rotation angle was varied, giving twice the resolution that could be obtained from the shift of a single peak. Both the fourfold and twofold anisotropies are easily visible in Fig. 13(b). The crosses correspond to BLS data and the solid curve has been calculated using the parameters determined from FMR. Good agreement between BLS and FMR is obtained. Because of the small sample area measured by BLS (area of $\sim 10^{-6}$ cm^2) compared with FMR (area of ~ 1 cm^2), agreement between the two techniques indicates that the bilayer samples were homogeneous on length scales larger than 10 μm.

For clean Ni/Fe interfaces the interlayer exchange coupling is expected to be strong and should result in FMR and BLS responses corresponding to the pure acoustic mode. It can be anticipated that the scaling formulas (11) should be followed. Epitaxially grown bilayers should borrow their magnetic properties from both the cubic Fe, which has a large saturation magnetization, and the "bcc Ni," which has a large in-plane fourfold anisotropy.[5] Indeed, the magnetic bilayers with 10-ML-thick Ni show a robust FMR signal with a strong in-plane fourfold anisotropy.

In the simplest case the bilayers interact only through the interface exchange coupling. In this limit the scaling laws are exactly valid and in principle magnetic properties of "bcc Ni" can be extracted from FMR and BLS measurements carried out on Ni/Fe bilayers and appropriate single Fe layers. However, real bilayers do not behave in this simple manner. The itinerant nature of valence electrons, which becomes particularly important when the bilayer thickness becomes comparable to the electron mean free path, assures that some of these properties will be affected by valence-band hybridization and valence-state interface localization. For example, very recent measurements[12] and calculations[8] showed that the perpendicular uniaxial surface anisotropy in ultrathin Fe films was strongly affected by the presence of noble metals in spite of the fact that their valence electrons hybridize only weakly with the Fe valence bands.

Analysis of FMR results obtained on epitaxially grown Ni/Fe bilayers was carried out assuming that the scaling

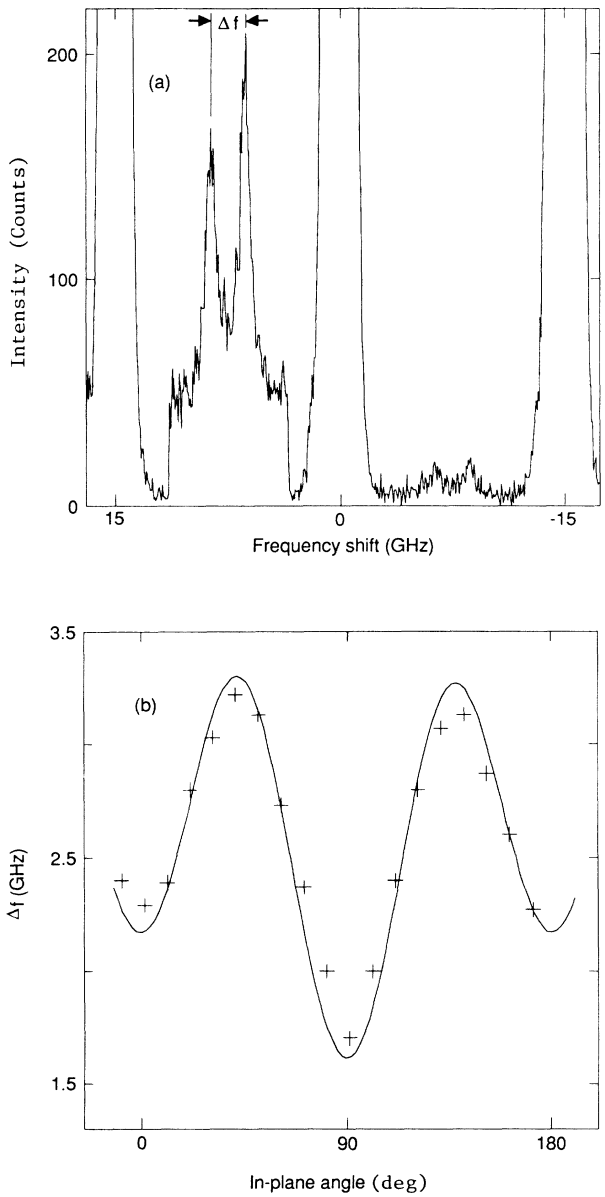

FIG. 13. (a) Brillouin light scattering spectrum for sample Ni/Fe(10/6) for an applied field of 3.99 kOe and an incident laser power of 125 mW. A single interferometer with a free spectral range of 15 GHz was used. The total counting time for each data point in the frequency range $+3.6-+11.4$ GHz was 4.584 s and the total counting time for all other data points was 0.458 s. The peaks at $+6.3$ and $+8.6$ GHz correspond to the same surface mode: the peak at $+6.3$ GHz is shifted up in frequency and belongs to the elastic peak at -15 GHz; the peak at $+8.6$ GHz is shifted down in frequency and belongs to the elastic peak at $+30$ GHz. The difference in frequency between the peaks shifted up and down is labeled Δf. (b) The frequency difference Δf as a function of the in-plane angle between the applied field and the crystal (100) axis for sample Ni/Fe(10/6). An applied field of 3.99 kOe and an incident laser power of 125 mW were used. The crosses are measured Brillouin light scattering data and the solid curve is calculated using the magnetic parameters determined from ferromagnetic resonance (see Table I). There was a shift of 0.98 ± 0.15 GHz between the measured and calculated values of Δf. The solid curve has been shifted upward by 0.98 GHz to overlay with the measured data.

laws were valid. The comparison of "bcc Ni" magnetic properties, obtained on different Ni/Fe bilayers, showed which of these magnetic parameters followed a simple bilayer scaling and which magnetic parameters were strongly affected by the collective nature of the valence electrons. Results of this analysis are presented in Table II. The scaling parameters α used in Table II were evaluated using the saturation magnetization of bulk Fe ($4\pi M_s = 21.55$ kG), and employed either the saturation magnetization of bulk fcc Ni ($4\pi M_s = 6.13$ kG) or the saturation magnetization of bcc Ni as theoretically predicted by Moruzzi *et al.*[27] ($4\pi M_s = 4.5$ kG). Epitaxially grown Ni layers in Ni/Fe(10.5/3.5), Ni/Fe(10/6), and Ni/Fe(9.4/5.7) bilayers were thicker than the critical thickness and therefore were reconstructed. These bilayers exhibited large fourfold anisotropies, see Table I. Note also that the fourfold anisotropy field scales extremely well (H_{K_1} agrees within 5% for the three bilayers with reconstructed Ni which is within the accuracy of the thickness measurements; see Table II).

At this point we explored whether magnetic properties of the pure unreconstructed bcc Ni could be found. The scaling law predicted that the fourfold anisotropy field in the Ni/Fe(3.5/5.6) sample should have been relatively large, $H_{K_1} = 250$ Oe, and easily measurable using FMR. FMR measurements at room and LN_2 temperatures, see Fig. 14, showed that the fourfold in-plane anisotropies in the Ni/Fe(3.5/5.6) sample were almost identical to those expected for a single 5.6-ML-thick Fe layer sandwiched between a Ag(001) substrate and a Au(001) cover layer; see Table I. Evidently the fourfold anisotropy in the pure bcc Ni is significantly smaller than that observed in lattice reconstructed Ni. Furthermore, all other properties of the Ni/Fe(3.5/5.6) bilayer were almost identical to those observed in the 5.6-ML-thick Fe film. Therefore we conclude tentatively that the pure unreconstructed bcc Ni is nonmagnetic, even at LN_2 temperatures.

The FMR linewidth, ΔH, in the samples Ni/Fe(10.5/3.5), Ni/Fe(10/6), and Ni/Fe(9.4/5.7) had a very large angular dependence with the narrowest lines along the [100] easy axes and the widest lines along the [110] hard axes; see Fig. 15. This contrasts sharply with all previous measurements carried out on Fe films where FMR linewidths were nearly isotropic. In fact, no similar large anisotropic behavior in ΔH has been observed in any $3d$ transition metals or their alloys.

The similarity between the angular dependence of ΔH and the FMR field is even more surprising; see Fig. 15. Obviously, the fourfold anisotropy energy and FMR line broadening have a common physical origin. The frequency dependence of ΔH in all samples studied showed a linear dependence with a zero-frequency offset $\Delta H(0)$; see Fig. 16. It has been shown[28] that the linear slope is proportional to the intrinsic Gilbert damping parameter and the frequency-independent offset $\Delta H(0)$ is caused by the presence of magnetic inhomogeneities in the sample; this is often referred to as the two-magnon scattering mechanism.[29]

The Gilbert damping in Ni/Fe(10.5/3.5) and Ni/Fe(10/6) samples is isotropic. It is the frequency-independent part $\Delta H(0)$ which shows a strong anisotropic behavior and which resembles the fourfold in-plane anisotropy field. It could be argued that the anisotropic ΔH behavior is a consequence of the lagging of the saturation magnetization behind the applied field. In this respect, BLS studies are particularly useful because the applied field is held constant and the spectra are obtained by sweeping the frequency. The BLS results shown in Fig. 17 prove that the anisotropic dependence of ΔH is dynamic in origin and is not caused by magnetostatic effects. Since the fourfold anisotropy and the anisotropy

TABLE II. Magnetic properties of ultrathin bcc Ni films grown on ultrathin bcc Fe(001) films deposited on bulk fcc Ag(001) substrates. The linewidths were calculated for a microwave frequency of 36.6 GHz using the scaling law.

Sample	$4\pi M_s$ (Ni) (kOe)	$(4\pi D_\perp M_s)_{\text{eff}}$ (kOe)	g	H_{K_1} (kOe)	H_{K_u} (kOe)	ΔH (expt. Fe)[c] (kOe) easy	ΔH (expt. Fe)[c] (kOe) hard	ΔH (selected Fe)[d] (kOe) easy	ΔH (selected Fe)[d] (kOe) hard
Magnetic properties of bcc Ni overlayers measured at room temperature ($T = 300$ K)									
(9.4 ML Ni)/(5.7 ML Fe)	6.14[a]	14.33	2.14	2.00	0.078	0.472	1.32	0.323	1.17
	4.50[b]	15.98	2.16	2.46	0.097	0.552	1.61	0.348	1.41
(10 ML Ni)/(6 ML Fe)	6.14[a]	13.22	2.12	2.06	0.36	0.590	1.602	0.408	1.385
	4.50[b]	14.5	2.13	2.52	0.44	0.701	1.964	0.445	1.614
(10.5 ML Ni)/(3.5 ML Fe)	6.14[a]	7.57	2.22	2.16	0.260	0.264	1.241	0.422	1.434
	4.50[b]	8.37	2.25	2.58	0.311	0.249	1.417	0.471	1.734
Magnetic properties of bcc Ni overlayers measured at liquid nitrogen temperature ($T = 77$ K)									
(10 ML Ni)/(6 ML Fe)	6.14[a]	9.737	2.131	5.876	0.523	0.760	3.183	0.497	2.919
	4.50[b]	9.88	2.14	7.256	0.622	0.910	3.931	0.551	3.572
(10.5 ML Ni)/(3.5 ML Fe)	6.14[a]	6.00	2.22	5.6	0.347	0.270	2.300	0.496	2.521
	4.50[b]	6.41	2.25	6.67	0.415	0.230	2.652	0.539	2.961

[a]The scaling calculation was carried out using the saturation magnetization corresponding to fcc Ni, $4\pi M_s = 6.14$ kOe.
[b]The scaling calculation was carried out using $4\pi M_s = 4.5$ kOe, the saturation magnetization corresponding to bcc Ni (Ref. 29).
[c]These FMR linewidths were calculated using the bilayer scaling law and the Fe film properties given in Table I.
[d]These FMR linewidths were calculated assuming the ΔH of a bilayer Fe films was 220 Oe at 300 K and 280 Oe at 77 K.

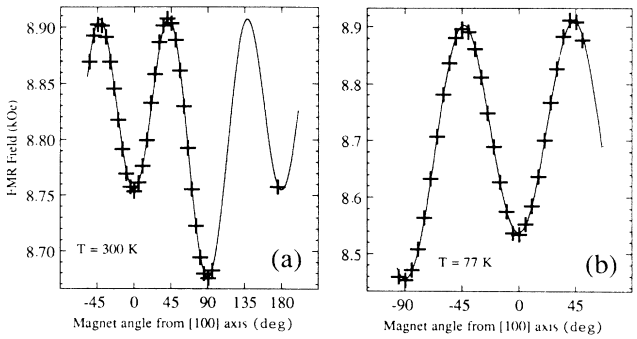

FIG. 14. The in-plane angular dependence of measured FMR field for the [15 ML Au(001)]/[3.5 ML Ni(001)]/[5.6 ML Fe(001)]/[bulk Ag(001)]/[sample Ni/Fe(3.5/5.6)]. (a) $f=36.615$ GHz, $H_{K_1}=0.126$ kOe, $H_{K_u}=-0.048$ kOe, twofold axis along the Fe[001] direction, g factor is 2.09, along the Fe[001] direction, g factor is 2.09, $(4\pi D_\perp M_s)_{\text{eff}}=8.92$ kG, $T=300$ K. (b) $f=36.745$ GHz, $H_{K_1}=0.271$ kOe, $H_{K_u}=-0.049$ kOe, twofold axis along the Fe [001] direction, g factor is 2.09, $(4\pi D_\perp M_s)_{\text{eff}}=9.29$ kG, $T=77$ K.

in $\Delta H(0)$ have a common origin, it follows that the strong fourfold in-plane anisotropy is not a consequence of the intrinsic spin-orbit interaction. Rather, it is a result of crystallographic defects generated during the Ni overlayer lattice relaxation.

As previously mentioned, small twofold in-plane anisotropies were observed in all epitaxial bilayers and in most of the ultrathin single Fe films grown on vicinal Ag substrates. Note that there is a significant decrease in this anisotropy in the sample Ni/Fe(9.4/5.7) and single Fe layers[12] grown on singular Ag substrates.

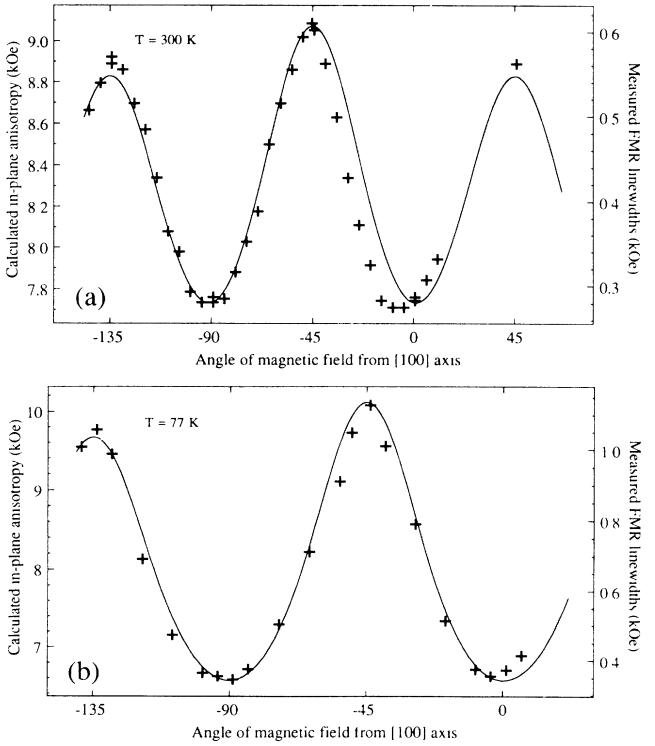

FIG. 15. The in-plane angular dependences of FMR linewidth for sample Ni/Fe(10/6) using the 36.6-GHz system at (a) room temperature and (b) LN_2 temperature. The superimposed solid curves in (a) and (b) were taken from Figs. 10(b) and 10(d), respectively, to demonstrate a similarity between the in-plane anisotropy of FMR field and linewidth.

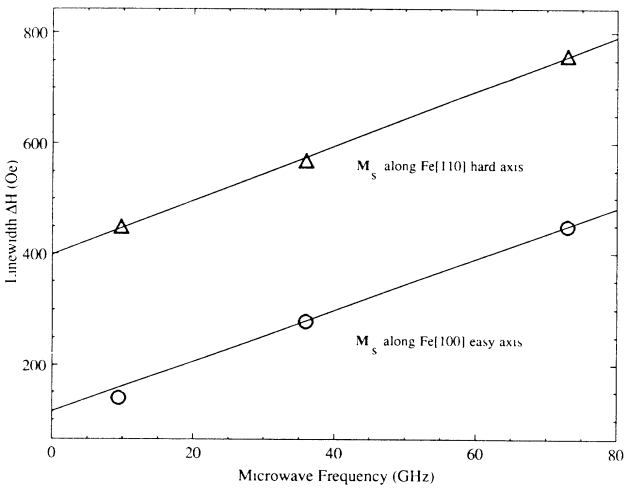

FIG. 16. The frequency dependence of FMR linewidth for sample Ni/Fe(10/6) at room temperature. The linewidth is linear with microwave frequency. The zero-frequency intercepts, $\Delta H(0)$, originate in sample inhomogeneities. The slopes of the solid lines are caused by the intrinsic Gilbert damping. Note that the intrinsic damping is almost isotropic whereas $\Delta H(0)$ exhibits a strong angular dependence. $\Delta H(0)$ along the easy axis is very small and is comparable to the narrowest FMR linewidths measured in thick epitaxial Fe films.

V. DISCUSSION OF RESULTS

Table II shows that for the fourfold in-plane anisotropy field in all reconstructed Ni/Fe bilayers satisfies the

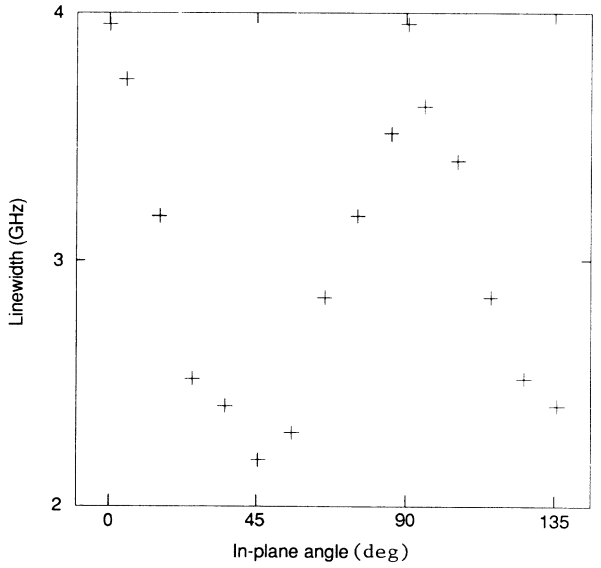

FIG. 17. Brillouin light scattering linewidth as a function of the in-plane angle between the applied field and the crystal (001) axis for sample Ni/Fe(10/6). An applied field of 6.81 kOe and an incident laser power of 125 mW were used.

bilayer scaling law given by Eq. (11) extremely well; see Table II, column 4. This is true for samples grown on both the singular and vicinal substrates. The fourfold anisotropy field, $H_{K_1}=2.6$ kOe, in a 10-ML-thick overlayer of "bcc Ni" is very close to that observed in a 60-Å-thick "bcc Ni" layer epitaxially grown on the bulk Fe substrate ($H_{K_1}=3.2$ kOe). Therefore, it is reasonable to assume that the observed large in-plane fourfold anisotropies belong to bulk properties of the reconstructed "bcc Ni."

Magnetostatic and magnetoelastic energies stored in growth defects become a part of the total magnetic energy and generate restoring torques of their own. However, well-defined in-plane fourfold anisotropy requires a corresponding degree of symmetry in the lattice defects. A network of mutually perpendicular misfit dislocations in (001) epitaxial structures has been previously observed[30] and could be the origin of the fourfold anisotropy. The lateral lattice relaxation (2%), observed by RHEED, suggests that the bcc Ni lattice parameter a_{Ni} is mismatched to the bcc Fe lattice parameter, a_{Fe}; see Sec. II. Therefore, after reaching the critical thickness, the Ni layer releases its elastic energy by introducing a network of in-plane edge misfit dislocations.[30] The lattice misfit, $\Delta a=a_{\mathrm{Ni}}-a_{\mathrm{Fe}}$, determines their linear densities, $a/\Delta a$, in either the [100],[010] or [110],[1 −1 0] crystallographic directions. This results in a "checkerboard" surface pattern which possesses the required symmetry for the behavior of the fourfold in-plane magnetic anisotropy and FMR linewidth. The easy axis of these anisotropies is along the [100] direction.

The other Ni parameters, such as $4\pi M_{\mathrm{eff}}$, g factor, and in-plane uniaxial anisotropies, do not scale well. Some parameters, like $4\pi M_{\mathrm{eff}}$ and g factor, are very dependent on the collective behavior of valence electrons and their lack of scaling is not surprising. Other parameters, like H_{K_u} and ΔH, are less easy to understand. However, all of these parameters have distinct trends worth noting.

The perpendicular uniaxial anisotropy decreases $\approx 10\%$ ($4\pi M_{\mathrm{eff}}$ increases) with decreasing temperature in all single Fe films covered by Au layers; see Table I. On the other hand, the Fe films covered by Ag(001) increase their perpendicular uniaxial anisotropy with decreasing temperature.[4] In this respect reconstructed bilayers behave like Fe films covered with Ag(001) and unreconstructed bilayers behave like Fe films covered with Au(001).

The in-plane twofold anisotropies in bilayers were enhanced by reconstructed Ni overlayers. For example, the sample Ni/Fe(10.5/3.5) with a 3.5-ML Fe film showed an appreciable in-plane anisotropy while no in-plane anisotropies were observed in the single 3.5-ML-thick Fe films. This increase is also accompanied by a rotation in the uniaxial axis (in all bilayers with reconstructed Ni) from the [100] to the [110] direction. The locking of the in-plane uniaxial anisotropies along major crystallographic axes is remarkable. However, it should be pointed out that the locking in some cases deviates by $\sim 10°$ from a principal axes, see Table I. The in-plane uniaxial anisotropy is appreciable only in samples grown on vicinal substrates and therefore is a consequence of the presence of atomic steps in the Ag substrate that break the symmetry of the fourfold (001) plane.

The mechanism of the in-plane uniaxial anisotropies can be discussed from two perspectives. Firstly, they can be caused by growth defects formed around atomic steps. In this case the lowest symmetry, the twofold in-plane uniaxial anisotropy [described by Eq. (4)], can be expected. Secondly, the broken symmetry of vicinal surfaces can result in an asymmetric fourfold anisotropy. Misfit dislocations may not form an ideal square array; e.g., they may have unequal dislocation densities in mutually perpendicular in-plane directions. The asymmetric in-plane fourfold anisotropy can be described by

$$E_{\mathrm{fourfold}}=-\tfrac{1}{2}(K_{1x}\alpha_x^4+K_{1y}\alpha_y^4)$$
$$=-\tfrac{1}{2}K_{1x}(\alpha_x^4+\alpha_y^4)-\tfrac{1}{2}K_F\alpha_y^4\ , \qquad (18)$$

where $K_F\equiv K_{1y}-K_{1x}$. This asymmetry results in an additional fourth-order in-plane uniaxial anisotropy which originates directly in the dominant fourfold anisotropy. Since the fourth-order anisotropy is locked to principal fourfold axes, the direction of the uniaxial axis along the [100] direction in single Fe bilayers is a direct consequence of this model.

We reanalyzed our data by using the fourth-order in-plane uniaxial anisotropy; see Table III. The angular dependence of the FMR field can be equally well fit for samples with the uniaxial axis locked closely to {100} and {110} axes. However, numerical fits were noticeably worse in samples with the uniaxial axis oriented away from the cubic principal axis. These fits can be improved by adding the second-order uniaxial anisotropy. However, the resulting in-plane fourfold and twofold anisotropies were not consistent for different microwave frequencies and therefore were rejected. Furthermore, the four-

TABLE III. Properties of Ni/Fe bilayers and single Fe overlayers at room and liquid-nitrogen temperatures when a fourth-order, in-plane anisotropy is assumed to be present.

Sample	Temp. (K)	$4\pi M_{\mathrm{eff}}$ (kG)	g	$2K_1/M_s$ (kOe)	$2K_F/M_s$ (kOe)
(3.5 ML Ni)/(5.6 ML Fe)	300	8.87	2.09	0.086	−0.039
	77	9.1	2.09	0.228	−0.042
(10 ML Ni)/(6 ML Fe)	300	10.9	2.097	0.657	0.119
	77	12.58	2.092	1.89	0.205
(10.5 ML Ni)/(3.5 ML Fe)	300	6.93	2.147	1.08	0.090
	77	8.79	2.147	2.69	0.126

fold uniaxial anisotropies have a significantly weaker temperature dependence than the main fourfold anisotropies. This would indicate that the fourfold and fourth-order uniaxial anisotropies are not caused by an identical mechanism. Therefore we believe that the uniaxial anisotropy is better described by the twofold in-plane anisotropy.

The bilayer g factor exhibits a simple behavior. With a decreasing Fe thickness, the bilayer g factor converges towards the fcc Ni value of $g=2.187$.[31] However, the bilayer g factor approaches the Fe value faster than expected from the scaling law, Eq. (11). This result clearly shows that Fe-Ni valence-band hybridization is indeed significant and affects the spin-orbit contribution to the overall valence-band behavior.

The FMR linewidth in the reconstructed bilayers Ni/Fe(10.5/3.5) and Ni/Fe(10/6) scales poorly. Deviations from the scaling law are more serious for results obtained for easy axes than hard axes. However, scaling predicts correctly that the Ni FMR linewidth is much larger when the magnetization points along the [110] direction than when it points along the [100] direction. The main reason for the discrepancy in scaling of FMR linewidths can be found by a reexamination of the data. Ni/Fe(10.5/3.5) and Ni/Fe(10/6) have almost identical FMR linewidths along the easy axis at both room and LN_2 temperatures, see Table I, whereas ΔH in a 3.5-ML-thick Fe single layer is almost twice that observed in the 6-ML-thick Fe single layer. Consequently the scaling law, Eq. (11), using the single-layer iron linewidths gives appreciably different values for the FMR linewidth of the two Ni overlayers even though they have almost the same thicknesses. However, if we assume that the FMR linewidths in both the 3.5-ML and 6-ML Fe layers were identical, then the Ni linewidth follows the scaling law; see columns 8 and 9 in Table II. Our previous measurements,[4] carried out on single Fe layers covered by Au(001) and Ag(001) overlayers, showed that FMR linewidths are sensitive to the particular interface. It is therefore possible that FMR linewidths in Fe layers are changed by contact with the Ni layers. FMR linewidths along the hard axis are dominated by misfit dislocations and hence we expect them to obey the bilayer scaling, as is observed for the fourfold anisotropy. However, this conclusion implies that the FMR linewidths in bilayer Fe layers are only weakly dependent on their thickness, contrary to the behavior of individual Fe layers in contact with Ag or Au.

We tried to observe the FMR and BLS resonance signals in the single 10-ML-thick bcc Ni layer epitaxially grown on a Ag(001) substrate, sample Ni(10), but none could be observed. The Ni(10) sample was difficult to study. Its large resonance damping and small saturation magnetization reduced FMR and BLS signals close to the detectable limits. The rougher surface of this Ni sample, see Sec. II, would lead to a further resonance line broadening and very likely resulted in our inability to measure its resonance peak.

For completeness, one has to entertain the idea that the reconstructed Ni is also nonmagnetic and all results are due to a possible propagation of misfit dislocations into the Fe layer. In the following paragraphs arguments will be brought forward to show that this is not the case.

Firstly, the bilayer scaling for the in-plane fourfold anisotropy works if the Ni overlayer is magnetic. Secondly, one should recall[6] that a 60-Å-thick overlayer of Ni, epitaxially grown on bulk Fe, exhibited almost the same value for $2K_1/M_s$ as the bilayers. However, let us assume that the in-plane fourfold anisotropy is caused by a reconstruction of the Fe layers. In this case, see Table I, the fourfold anisotropy decreases in bilayers as the Fe layer thickness increases. Then, assuming a linear dependence of anisotropy with thickness, the fourfold anisotropy would be negligible approximately 15 Å away from the Ni/bulk Fe interface with an average value $H_{K_s}\sim 0.7$ kOe. Therefore surface misfit dislocations in Fe(001) bulk substrates would result in a surface pinning with $K_s\sim(0.7\text{kOE})(M_s)(15\text{ Å})=0.2$ ergs/cm^2. FMR calculations, using the above-estimated K_s, show that the FMR field, oriented along the easy axis, would shift to lower field. This is contrary to our observations obtained for Ni on bulk Fe.[6] Along the hard axis the calculated FMR field is shifted upwards as in the Ni/bulk Fe experiments, but the calculated shift is significantly smaller than the observed one. Furthermore, it should be emphasized that the above estimate of K_s is grossly exaggerated. The bulk Fe surface is very likely weakly affected by the Ni lattice reconstruction. It is, after all, predominantly elastic energy stored in the pure bcc Ni which is released by misfit dislocations; therefore the lattice reconstruction of the stable bulk bcc Fe should be rather minimal.

We believe that the experimental results, obtained on ultrathin bilayers and Ni layers on bulk iron, strongly support our original interference: the reconstructed "bcc Ni" is magnetic and possesses a large in-plane fourfold anisotropy.

Another interesting aspect of sample Ni/Fe(10/6) is the observation of hysteresis with much smaller coercive fields than H_{K_1}. This proves the existence of domains in this ultrathin sample. The microwave absorption at 9.5 GHz near zero field, with the dc field along the easy axis, is shown in Fig. 18. The FMR peak is shifted to low fields by the large cubic crystalline anisotropy. The loop is actually defined by the tails of the FMR peaks which occur on either side of zero field. The coercive field is ~ 25 Oe whereas $H_{K_1}\sim 770$ Oe. Thus the domains nucleate in the sample at very low fields (~ 13 Oe) and spread easily through the sample to reverse the magnetization.

VI. CONCLUSIONS

We have successfully grown epitaxial ultrathin Fe/Ni bilayers on Ag(001) bulk substrates. RHEED studies showed that Ni films less than 6 ML thick grow homomorphously in the pure bcc structure when epitaxially grown on Fe(001). Lattice reconstructions, which follow after the Ni overlayers reach a critical thickness, suggest that the equilibrium atomic spacing of the metastable bcc Ni does not exactly match the Fe(001) spacing.

Magnetic properties of the Fe/Ni bilayers were investi-

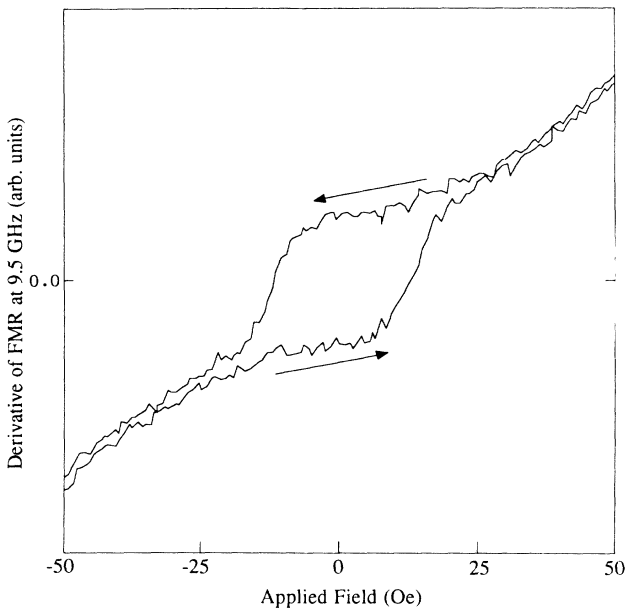

FIG. 18. Hysteresis in FMR from sample Ni/Fe(10/6) at 9.5 GHz with the applied field along the easy axis [Fe(001)]. $H_{K_1}=770$ Oe for this sample while the coercive field is ~ 25 Oe. The arrows show the directions in which the applied field was swept.

gated using FMR and BLS. The lattice-reconstructed Fe/Ni bilayers exhibited large in-plane fourfold anisotropies. This is in sharp contrast with single Fe layers for which the fourfold in-plane cubic anisotropy decreases with the Fe layer thickness and becomes negligible in 3–4-ML-thick films.

The in-plane angular dependence of the FMR field and FMR linewidth helped to identify the origin of the fourfold in-plane anisotropy. Large fourfold anisotropies observed in Fe/Ni bilayers do not originate in the intrinsic spin-orbit contribution to the valence-electron energy bands, but are a consequence of lattice reconstruction. The pure bcc Ni overlayer does not contribute to fourfold in-plane magnetic anisotropies. In fact unreconstructed Ni layers play a very minor role in bilayer magnetic properties and therefore are very likely nonmagnetic even at LN_2 temperatures.

At clean Fe/Ni interfaces the interlayer exchange is strong and results in a tightly coupled system. A theory of exchange-coupled bilayers was formulated. It was shown that the effective fields of individual layers form a set of natural variables; the bilayer effective fields are expressed as a linear combination of the scaled effective fields of the individual layers; see Eq. (11). The scaling parameter α, for a particular layer, is given by the product of the magnetic moment per atom and the number of atomic planes in the layer. The validity of scaling is limited to the simplest interlayer interaction in which only Heisenberg-like exchange coupling plays a role. The itinerant nature of valence electrons in $3d$ transition metals assures that some magnetic properties are strongly affected by valence-band interlayer hybridization. The compliance of bilayer magnetic properties with scaling was checked by comparison of "bcc Ni" magnetic properties obtained on different Ni/Fe bilayers. We found that the scaling in ultrathin Fe/Ni bilayers is satisfied remarkably well for the fourfold in-plane anisotropy field at both room and LN_2 temperatures. However, the perpendicular and in-plane uniaxial anisotropies, g factor, and resonance linewidths did not satisfy the scaling law because they are strongly affected by $3d$ interband hybridization.

Magnetostatic and magnetoelastic energies, stored in growth defects during the Ni reconstruction, contributed to the total magnetic energies and resulted in effective fields which affected the magnetic response. It is very surprising that growth defects can create well-defined in-plane anisotropies which surpassed those originating in the spin-orbit mechanism. Apparently the network of misfit dislocations in the (001) plane formed a checkerboard surface pattern. This pattern possessed the required fourfold symmetry and therefore could be responsible for the observed fourfold magnetic anisotropies. Furthermore, as a consequence of the scaling property, it is possible to control the strength of the fourfold anisotropies by choice of the layer materials and thicknesses. In-plane uniaxial anisotropies were observed in all samples grown in vicinal Ag(001) substrates. The samples prepared on singular surfaces exhibited a negligible in-plane uniaxial anisotropy and therefore the in-plane uniaxial anisotropies originated in the Ag atomic steps. Other magnetic properties such as $(4\pi D_{\perp}M_s)_{\text{eff}}$, g factor, and particularly the in-plane fourfold anisotropy are very weakly dependent on the density of atomic steps of the Ag substrates.

The ability to control quantitatively magnetic properties is one of the ultimate goals facing the magnetic community working with MBE technologies. In this respect we believe that the results of our studies on ultrathin Fe/Ni bilayers have helped to advance the atomic engineering of new magnetic structures.

ACKNOWLEDGMENTS

The authors would like to thank the National Research Council of Canada for financial support and Ken Myrtle for technical assistance in MBE and FMR.

APPENDIX: DIPOLE FIELDS ON THE ATOMIC SCALE

The magnetic field from a square lattice of aligned dipoles in a single atomic plane does not vanish even though it does outside of a continuum slab. To calculate the demagnetizing field acting against the rotation of the dipoles into the perpendicular to the plane, it is sufficient to calculate the dipolar field with the moments perpendicular to the plane and then multiply by $\frac{3}{2}$. To calculate the demagnetizing field acting in the plane, one removes an atom. To calculate the demagnetizing field acting on another plane, one removes the plane and adds the effects from all other planes plus the demagnetizing field from that plane. The field is spatially periodic at any distance z from the plane. Each harmonic falls off from the plane as $\exp(-2\pi nz/a)$, where $a=a_0/\sqrt{2}$ is the spacing of the square lattice for a bcc lattice with lattice parameter a_0.

The factor of 2π in the exponential assures the rapid dominance of the first harmonic. Beyond the second-neighbor distance above the plane, the first harmonic is completely dominant for practical purposes.

The field can be found by selecting a disk of dipoles and summing them. The contribution from the rest of the plane can be found by integration of a continuum starting at a radius slightly larger than that of the disk. That radius is determined by requiring that the dipole sum plus the integral falls at the rate of the first harmonic, in a region where the first harmonic dominates.

The demagnetizing field acting on an atom in the plane is $-0.539\,154\,6(4\pi M_s)$. The demagnetizing field from one plane acting on an atom in the center bcc position above a single atomic layer is $-0.249\,259\,8(4\pi M_s)$. The demagnetizing field from one plane at an atom position on the corner of the bcc lattice directly above an atom in the single atomic layer is $0.019\,544\,1\exp[-2\pi(n-2)/\sqrt{2}](4\pi M_s)$, where n, corresponding to the number of layers above the atom plane, takes even values. The demagnetizing fields at center positions, except in the first layer above the atom plane, are given by $-0.000\,738\,8\exp[-2\pi(n-3)/\sqrt{2}](4\pi M_s)$, where n takes odd values.

The demagnetizing factors are as follows.

(a) For a single layer: $-0.539\,154\,6$.

(b) For two layers: $-0.788\,414\,4$.

(c) For three layers: the central layer, $-1.037\,674\,2$; the top and bottom layers, $-0.768\,870\,3$; average demagnetizing factor, $-0.858\,471\,6$.

(d) for four layers: the inside two layers, $-1.018\,130\,1$; the top and bottom layers, $-0.769\,609\,1$; average demagnetizing factor, $-0.893\,869\,6$, etc.

The average demagnetizing factor for a layer with n atomic planes in the bcc lattice is given by $D=1-0.4245/n$, for all n beyond $n=2$.

---

[1]The quotation marks are intentional, see Sec. II for details.

[2]Ultrathin layers (films or overlayers) will be used to refer to any epitaxially grown structure thinner than the exchange length defined as $[A_{ex}/(2\pi M_s^2)]^{1/2}\approx 33$ Å.

[3]B. Heinrich, K. B. Urquhart, A. S. Arrott, J. F. Cochran, K. Myrtle, and S. T. Purcell, Phys. Rev. Lett. **59**, 1756 (1987).

[4]B. Heinrich, K. B. Urquhart, J. R. Dutcher, S. T. Purcell, J. F. Cochran, A. S. Arrott, D. A. Steigerwald, and W. F. Egelhoff, Jr., J. Appl. Phys. **63**, 3863 (1988).

[5]B. Heinrich, A. S. Arrott, J. F. Cochran, S. T. Purcell, K. B. Urquhart, N. Alberding, and C. Liu, in *Thin Film Techniques for Low Dimensional Structures,* NATO ASI Series, edited by R. F. C. Farrow, S. S. Parkin, P. J. Dobson, J. H. Neave, and A. S. Arrott (Plenum, New York, 1987).

[6]B. Heinrich, A. S. Arrott, J. F. Cochran, S. T. Purcell, K. B. Urquhart, and K. Myrtle, J. Cryst. Growth **81**, 562 (1987).

[7]B. T. Jonker, K.-H. Walker, E. Kisker, G. A. Prinz, and C. Carbone, Phys. Rev. Lett. **57**, 142 (1986).

[8]J. G. Gay and R. Richter, J. Appl. Phys. **61**, 3362 (1987).

[9]M. Stampononi, A. Vaterlaus, M. Aeschlimann, and F. Meier, Phys. Rev. Lett. **59**, 2483 (1987).

[10]J. J. Krebs, B. T. Jonker, and G. A. Prinz, J. Appl. Phys. **63**, 3467 (1988).

[11]F. A. Volkening, B. T. Jonker, J. J. Krebs, N. C. Koon, and G. A. Prinz, J. Appl. Phys. **63**, 3869 (1988).

[12]K. B. Urquhart, B. Heinrich, J. F. Cochran, and A. S. Arrott, in *Proceedings of the Joint MMM-Intermag Conference, Vancouver, 1988* [J. Appl. Phys. (to be published)].

[13]J. F. Cochran, B. Heinrich, and A. S. Arrott, Phys. Rev. B **34**, 7788 (1988).

[14]R. L. Lyles, Jr., S. J. Rothman, and W. Jager, Metallography **11**, 363 (1978).

[15]The sample surfaces that are more than 0.5° or less than 0.5° misoriented from a low-index plane are termed vicinal or singular surfaces, respectively.

[16]Z. Q. Wang, Y. S. Li, F. Jona, and P. M. Marcus, Solid State Commun. **61**, 623 (1987).

[17]A. A. Chernov, *Modern Crystallography III-Crystal Growth* (Springer-Verlag, Berlin, 1984), p. 99.

[18]M. A. Van Hove and G. A. Somorjai, Surf. Sci. **92**, 489 (1980).

[19]N. Raj and D. R. Tilley, Phys. Rev. B **36**, 7003 (1987).

[20]N. S. Almeida and D. L. Mills (unpublished).

[21]A. G. Gurevich, *Ferrites at Microwave Frequencies* (Consultants Bureau, New York, 1963).

[22]P. A. Grünberg, J. Appl. Phys. **57**, 3673 (1985).

[23]J. F. Cochran and J. R. Dutcher, in Ref. 12.

[24]K. Vayhinger and H. Kronmüller, J. Magn. Magn. Mater. **72**, 307 (1988).

[25]S. T. Purcell, B. Heinrich, and A. S. Arrott, in Ref. 12.

[26]J. R. Dutcher, J. F. Cochran, B. Heinrich, and A. S. Arrott, in Ref. 12.

[27]V. L. Moruzzi, P. M. Marcus, K. Schwarz, and P. Mohn, Phys. Rev. B **34**, 1748 (1986).

[28]J. F. Cochran, K. Myrtle, and B. Heinrich, J. Appl. Phys. **53**, 2261 (1982); B. Heinrich, J. F. Cochran, and R. Hasegawa, J. Appl. Phys. **57**, 3690 (1985).

[29]M. Sparks, *Ferromagnetic Relaxation Theory* (McGraw-Hill, New York 1964).

[30]M. J. Stowell, in *Epitaxial Growth B,* edited by J. W. Matthews (Academic, New York 1975).

[31]G. Dewar, B. Heinrich, and J. F. Cochran, Can. J. Phys. **55**, 821 (1977).

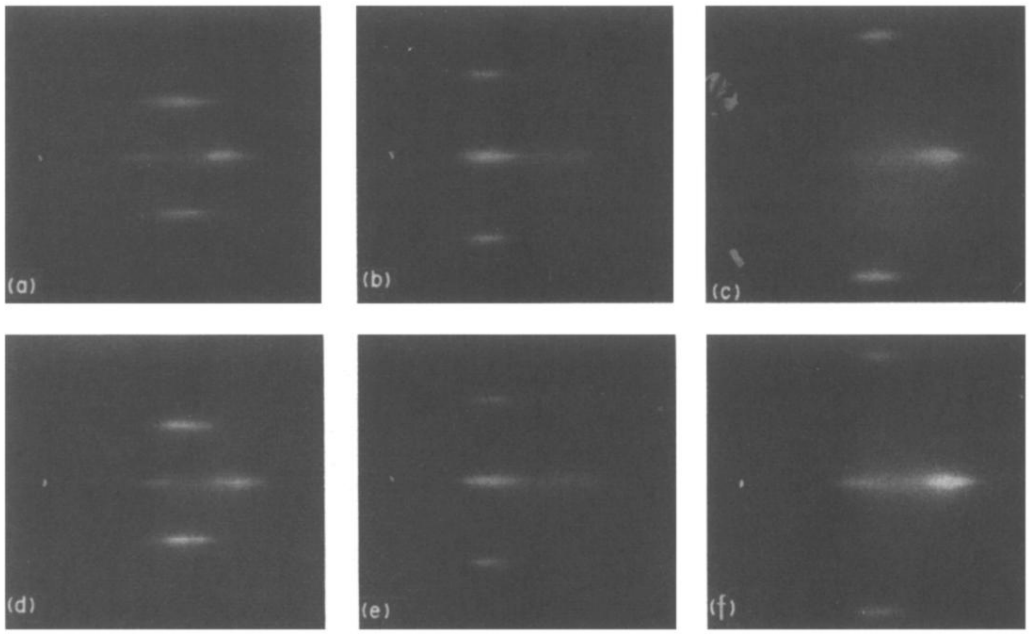

FIG. 1. RHEED patterns from 5.6 ML of Fe on Ag(001) [(a)–(c)] and 3.5 ML of Ni on the 5.6 ML Fe on Ag(001) [(d)–(f)]. The incident electron beam (10 kV) is along the Fe[100] azimuth in photos (a) and (d), the Fe[110] azimuth in (b) and (e), and the Fe [120] in (c) and (f). The RHEED photos show the surface to be a square array having the bulk Fe lattice spacing. The Ni on Fe on Ag patterns are almost identical to the Fe on Ag patterns with no extra diffraction streaks.

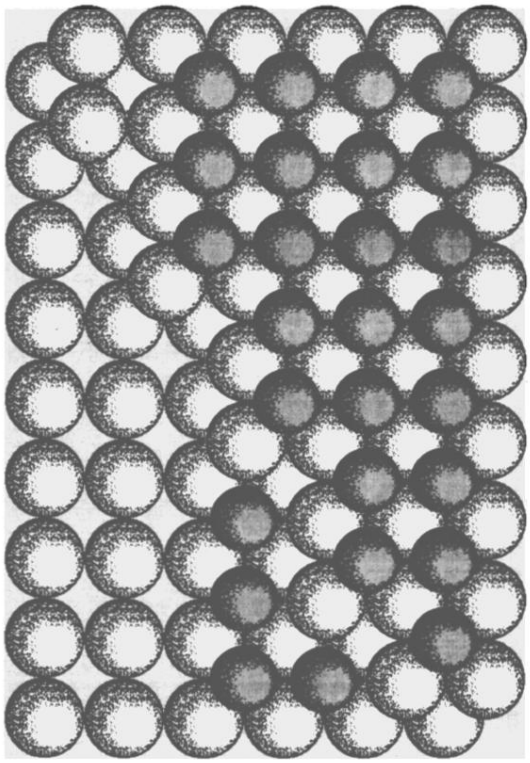

(a)

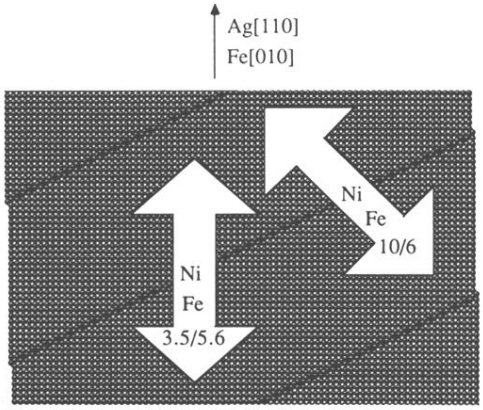

(b)

FIG. 5. (a) A detailed top view of the Ag(3 1 100) vicinal surface (large balls) covered by Fe atoms (small balls). The kinked atomic steps are oriented along the [120] Fe direction. Note that the Fe stacking along the surface steps is imperfect due to the large Ag atoms. (b) An idealized global view of the Ag(3 1 100) vicinal surface (each square represents an atom). The vicinal surface can be described as a descending staircase of atomic terraces. The arrows indicate the direction of locked in-plane uniaxial easy axis of reconstructed Ni/Fe(10/6) and unreconstructed Ni/Fe(3.5/5.6) bilayers. The orientation of the axes with respect to the theoretical description is shown in Fig. 6.

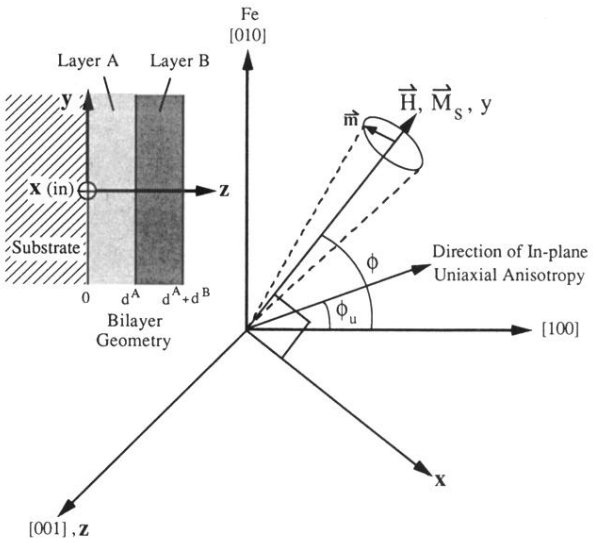

FIG. 6. Coordinate system used for the theory of eigenmodes of bilayers (Sec. III). Angles are measured positive *clockwise* from the [100] direction and therefore the angles ϕ and ϕ_u shown in the figure are negative.